Monthly Notices of the ROYAL ASTRONOMICAL SOCIETY

MNRAS **497,** 130–145 (2020)
Advance Access publication 2020 July 2

doi:10.1093/mnras/staa1892

Gaia white dwarfs within 40 pc – I. Spectroscopic observations of new candidates

P.-E. Tremblay,[1]★ M. A. Hollands,[1] N. P. Gentile Fusillo,[1,2] J. McCleery,[1] P. Izquierdo,[3,4] B. T. Gänsicke,[1] E. Cukanovaite,[1] D. Koester,[5] W. R. Brown,[6] S. Charpinet,[7] T. Cunningham,[1] J. Farihi,[8] N. Giammichele,[7] V. van Grootel,[9] J. J. Hermes,[10] M. J. Hoskin,[1] S. Jordan,[11] S. O. Kepler,[12] S. J. Kleinman,[13] C. J. Manser,[1] T. R. Marsh,[1] D. de Martino,[14] A. Nitta,[13] S. G. Parsons,[15] I. Pelisoli,[16] R. Raddi,[17] A. Rebassa-Mansergas,[17,18] J.-J. Ren,[19] M. R. Schreiber,[20,21] R. Silvotti,[22] O. Toloza,[1] S. Toonen[23] and S. Torres[17,18]

Affiliations are listed at the end of the paper

Accepted 2020 June 25. Received 2020 June 23; in original form 2020 May 11

ABSTRACT

We present a spectroscopic survey of 230 white dwarf candidates within 40 pc of the Sun from the William Herschel Telescope and Gran Telescopio Canarias. All candidates were selected from *Gaia* Data Release 2 (DR2) and in almost all cases, had no prior spectroscopic classifications. We find a total of 191 confirmed white dwarfs and 39 main-sequence star contaminants. The majority of stellar remnants in the sample are relatively cool ($\langle T_{\rm eff}\rangle = 6200$ K), showing either hydrogen Balmer lines or a featureless spectrum, corresponding to 89 DA and 76 DC white dwarfs, respectively. We also recover two DBA white dwarfs and 9–10 magnetic remnants. We find two carbon-bearing DQ stars and 14 new metal-rich white dwarfs. This includes the possible detection of the first ultra-cool white dwarf with metal lines. We describe three DZ stars for which we find at least four different metal species, including one that is strongly Fe- and Ni-rich, indicative of the accretion of a planetesimal with core-Earth composition. We find one extremely massive (1.31 ± 0.01 M$_\odot$) DA white dwarf showing weak Balmer lines, possibly indicating stellar magnetism. Another white dwarf shows strong Balmer line emission but no infrared excess, suggesting a low-mass sub-stellar companion. A high spectroscopic completeness (>99 per cent) has now been reached for *Gaia* DR2 sources within 40-pc sample, in the Northern hemisphere ($\delta > 0^\circ$) and located on the white dwarf cooling track in the Hertzsprung–Russell diagram. A statistical study of the full northern sample is presented in a companion paper.

Key words: stars: statistics – white dwarfs – solar neighbourhood.

1 INTRODUCTION

The nearest stars to the Sun and the Solar system have a remarkable historical importance in astronomy and continue to represent some of the best known examples of spectral types and exoplanetary hosts. Past efforts have generally been focused on the relatively small volume complete sample of ≈315 systems including main-sequence stars, brown dwarfs, white dwarfs, and planets within 10 pc of the Sun (Henry et al. 2018). White dwarfs make up about 6 per cent of stellar objects in that sample, but up to 95 per cent of local stars and their planetary systems are destined to that ultimate fate. These abundant stellar remnants serve several distinctive purposes in modern astrophysics such as tracing the local and Galactic stellar formation history (Winget et al. 1987; Rowell 2013; Tremblay et al. 2014; Fantin et al. 2019) and calibrating stellar ages (Rebassa-Mansergas et al. 2016; Fouesneau et al. 2019). The significance of these results is enhanced from unbiased volume-limited samples upon which statistical studies can be performed (Holberg, Oswalt & Sion 2002; Giammichele, Bergeron & Dufour 2012; Limoges, Bergeron & Lépine 2015; Holberg et al. 2016; Subasavage et al. 2017; Hollands et al. 2018b).

Some of the closest white dwarfs are prototypes for several wide ranging applications. The brightest and closest stellar remnant Sirius B has led to important input on stellar evolution and white dwarf structure (Bond et al. 2017), fundamental physics through gravitational redshift measurements (Joyce et al. 2018) as well as providing insight on the local binary population (Holberg et al. 2013; Toonen et al. 2017). GRW +70 8247, at 12.9 pc, was the first white dwarf to show circularly polarized light from its strong magnetic field (Kemp et al. 1970; Bagnulo & Landstreet 2019). The first degenerate star with metal lines in its spectrum, now recognized as the signature of a planetary system, was detected in the closest single white dwarf Van Maanen 2 (van Maanen 1917). Seventy years later, G29–38, a ZZ Ceti pulsator at 17.5 pc, became the prototype for white dwarfs with dusty debris discs (Zuckerman & Becklin 1987), leading to a very active research area around evolved planetary systems (Veras 2016) and a unique window into the bulk composition of other rocky worlds (Zuckerman et al. 2007). With increasing distances, further

★ E-mail: p-e.tremblay@warwick.ac.uk

rare examples of stellar or planetary evolution are being discovered, such as double white dwarf merger remnants (Hollands et al. 2020; Kawka, Vennes & Ferrario 2020b), extremely low mass white dwarfs that will most likely merge (Brown et al. 2016; Kawka et al. 2020a), or stellar remnants with transiting planetesimals and planets on close-in orbits (Vanderburg et al. 2015; Gänsicke et al. 2019; Manser et al. 2019). Hot white dwarfs might even serve to study the composition of gas giant planet atmospheres (Schreiber et al. 2019). A proper characterization of the occurrence of these systems requires the definition of larger volume-complete samples.

The *Gaia* spacecraft has shed a new light on the nearby Milky Way stellar population from its extremely accurate astrometry and photometry (Gaia Collaboration et al. 2018a). The Hertzsprung–Russell (HR) diagram of the local stellar population within 100 pc constructed from *Gaia* DR2 (Gaia Collaboration et al. 2018b) presents, for the first time, a near volume-complete census inclusive of all low-luminosity stars and white dwarfs. While the increase in size is exemplary, a full understanding of the local white dwarf population is still a major challenge. *Gaia* DR2 has significant technical limitations even within 100 pc, with a number of problematic sources that have been filtered from most early science results (Jiménez-Esteban et al. 2018; Gaia Collaboration et al. 2018b; Gentile Fusillo et al. 2019). We nevertheless estimate the completeness of the *Gaia* DR2 white dwarf selection to be ≈96 per cent within 20–40 pc (Hollands et al. 2018b; Gentile Fusillo et al. 2019; McCleery et al. 2020). Furthermore, only ≈10 per cent of *Gaia* white dwarfs within 100 pc have published spectroscopy (Gentile Fusillo et al. 2019; Tremblay et al. 2019b). Effective temperatures ($T_{\rm eff}$), surface gravities, and masses can, in principle, be derived from *Gaia* DR2 astrometry and photometry with a high precision of 1–2 per cent for nearby white dwarfs where reddening is small or negligible (Hollands et al. 2018b; Bergeron et al. 2019; Tremblay et al. 2019a). This technique is based on relatively well constrained white dwarf evolution models but the atmospheric composition must be known to transform colours into an atmospheric temperature. Erroneously assuming pure-hydrogen or pure-helium atmospheres can lead to 5–20 per cent systematic errors in mass (Bergeron et al. 2019) and a strong bias in the evaluation of total ages. Upcoming multi-object medium resolution spectroscopic follow-ups such as WEAVE, 4MOST, DESI, and SDSS-V (Dalton et al. 2014; DESI Collaboration et al. 2016; Kollmeier et al. 2017; de Jong et al. 2019), and to a lesser degree upcoming *Gaia* low-resolution spectrophotometry (Carrasco et al. 2014), will be essential to improve the accuracy of local white dwarf parameters and detect subtypes corresponding to metal pollution, magnetic fields or binarity. Nevertheless, it will be many years before these surveys cover large enough areas of the sky to significantly overlap with the ≈100-pc *Gaia* defined volume-limited white dwarf sample.

In this work, we describe our dedicated spectroscopic follow-up and analysis of new *Gaia* white dwarf candidates within 40 pc with the William Herschel Telescope (WHT) and Gran Telescopio Canarias (GTC). This directly follows upon the previous survey of Limoges et al. (2015), who relied on reduced proper motion for white dwarf identification. We discuss the nature of 230 *Gaia* white dwarf candidates across all sky, among which a handful were recently confirmed separately in the literature (see, e.g. Scholz et al. 2018; Landstreet & Bagnulo 2019, 2020) or had earlier ambiguous classifications. Among all observed targets, 155 are located in the Northern hemisphere ($\delta > 0\,^{\circ}$). Combining this work and existing spectroscopic confirmations from the literature, there are 521 spectroscopically confirmed white dwarfs found within *Gaia* DR2 in the Northern 40-pc hemisphere and only three unobserved high-probability white dwarf candidates (Gentile Fusillo et al. 2019), indicating a very high spectroscopic completeness. A detailed statistical analysis of the full northern 40-pc white dwarf sample, including a list of spectral types and references, is presented in a companion paper (Paper II; McCleery et al. 2020). Here, we also report on spectroscopic data of an additional 75 *Gaia* white dwarf candidates in the Southern hemisphere, which leaves approximately 200 unobserved high-probability white dwarf candidates in that region of the sky. The southern 40-pc sample will be part of a future statistical analysis once spectroscopic completeness has reached a higher level.

2 OBSERVATIONS

2.1 Catalogue photometry and astrometry

Gentile Fusillo et al. (2019) used spectroscopically confirmed white dwarfs from the Sloan Digital Sky Survey (SDSS) to map the regions of the *Gaia* DR2 HR diagram encompassed by these stellar remnants. Based on the fraction of SDSS white dwarfs and contaminants, they calculated a probability of being a white dwarf ($P_{\rm WD}$) for all *Gaia* sources that passed the initial selection. The authors recommend using $P_{\rm WD} > 0.75$ as a balance between completeness and contamination, a cut which recovers 96 per cent of the spectroscopically confirmed SDSS white dwarfs in the catalogue at all distances and up to a *Gaia* magnitude limit of $G \approx 20$.

We selected white dwarf candidates from the catalogue of Gentile Fusillo et al. (2019) with $\varpi > 25\,{\rm mas} \pm 1\sigma$ as the only requirement, resulting in 1233 sources, among which 184 are low probability candidates ($P_{\rm WD} < 0.75$). The following step was to perform a detailed cross-match of the literature to identify previous spectroscopic classifications. We have found 410 and 256 white dwarfs with a published spectral type in the Northern and Southern hemispheres, respectively, that we generally did not attempt to re-observe unless the spectral type was ambiguous or the spectrum not published (see Paper II for spectral types and references). The highest priority was given to high-probability candidates without a spectral type in the Northern hemisphere. We, nevertheless, kept low-probability candidates in our target list, especially those with high proper motions that might reveal to be peculiar white dwarfs. In addition to 155 sources selected in the Northern hemisphere, we also had the opportunity to observe an additional 75 *Gaia* white dwarf candidates in the Southern hemisphere. We use the WD J naming convention introduced by Gentile Fusillo et al. (2019) throughout all tables and figures, although we employ short names in the text for readability.

2.2 Spectroscopy

We observed a total of 230 white dwarf candidates at the Observatorio del Roque de los Muchachos, both with the Intermediate-dispersion Spectrograph and Imaging System (ISIS) on the WHT and the Optical System for Imaging and low-Resolution Integrated Spectroscopy (OSIRIS) on the GTC. Table 1 summarizes the different observations. Time was obtained through the International Time Programme ITP08 (PI Tremblay) and individual allocations (PIs Izquierdo, Marsh, Manser, and Gänsicke, see Table 1).

ISIS allows simultaneous observations using blue (R600B grating, R ≈ 2000) and red (R600R grating, R ≈ 3900) optimized CCDs via a dichroic beam-splitter. In our initial setup, we employed central wavelengths of 4540 and 6562 Å for the blue and red arms, respectively, ensuring coverage of all Balmer lines and Ca H+K lines

Table 1. Observing log.

Dates –	Telescope/ Instrument	Programme ID –	Grating –	Number of objects in this work
2016–2017	FAST	–	Fabricant et al. (1998)	3
–	LAMOST	–	Cui et al. (2012)	2
2018 July–December	GTC/OSIRIS	ITP08	R1000B, R2500R	26
2018 August 6–7	WHT/ISIS	C117	R600B, R600R	31
2018 August 9–23	WHT/ISIS	ITP08	R600B, R600R	67
2018 August 28–September 4	WHT/ISIS	P8/N13	R600B, R600R	3
2018 October 13–15	WHT/ISIS	ITP08	R600B, R600R	22
2019 February 9–10	WHT/ISIS	P9	R600B, R600R	29
2019 February 21–26	WHT/ISIS	ITP08	R600B, R600R	23
2019 April 13–14	WHT/ISIS	ITP08	R600B, R600R	6
2019 July 3–5	WHT/ISIS	C82	R600B, R600R	16
2019 Aug 1–3	WHT/ISIS	P23	R600B, R600R	2

Selected observations from FAST and LAMOST are included to ensure a coverage as complete as possible of *Gaia* DR2 white dwarfs in the Northern hemisphere (see Paper II).

(wavelength ranges ≈3730–5350, 5730–7290 Å). Objects with metal lines were typically re-observed with central wavelengths of 3930 and 8200 Å for the blue and red arms, respectively, to ensure maximal wavelength coverage from the limit of atmospheric transmission to 9000 Å. Slit width varied between 1 and 1.5 arcsec depending on the observing conditions and we employed a binning of 2 × 2, resulting in an average resolution of ≈2 Å. As much as possible, we tried to adjust exposure times to ensure signal-to-noise ratio (S/N) greater than 30 at Hα, but there is a correlation between S/N and apparent magnitude. Cool and featureless DC white dwarfs ($T_{\rm eff} < 4800$ K) have on average slightly lower S/N ratios.

Amongst the faintest sources in our target list, 26 candidates were observed with OSIRIS. Slit width was 1 arcsec and we employed the standard binning of 2 × 2. For objects with the reddest colours corresponding to *Gaia* $T_{\rm eff} \lesssim 4500$ K, we favoured low-resolution identification spectra using the R500B grating ($R \approx 540$, wavelength range 3600–7200 Å), which minimized overheads. For a few warmer objects, we favoured the R1000R grating ($R \approx 1100$, wavelength range 5100–10 000 Å) in order to possibly detect Hα. One DZ white dwarf was serendipitously discovered using this second setup (WD J1922+0233). It implies other metal lines are likely to be present in the unobserved blue portion of the spectrum, which would allow a detailed chemical abundance analysis.

The spectra were de-biased and flat-fielded using the standard STARKLINK[1] packages KAPPA, FIGARO, and CONVERT. We carried out optimal extraction of spectra using the package PAMELA[2] (Marsh 1989). The extracted 1D spectra were wavelength calibrated and flux calibrated using MOLLY (Marsh 2019).

We also rely on external spectroscopic observations for five additional *Gaia* white dwarfs in the Northern hemisphere for which we could not find a spectral type in the literature. Those were included to ensure a coverage as complete as possible of white dwarfs in the Northern hemisphere for the statistical analysis in the companion Paper II. Three spectra (WD J02215+0445, WD J0925+6120, and WDJ 0319+4230) were acquired at the 1.5-m Fred Lawrence Whipple Observatory telescope with the FAST spectrograph (Fabricant et al. 1998) using the 600 l/mm grating and the 1.5-arcsec slit, which provides 3550–5500 Å wavelength coverage at 1.7 Å spectral resolution. Two spectra (WD J0657+0550 and WD J0723+1617) were acquired from the LAMOST survey (Cui et al. 2012), which provides 3800–8800 Å wavelength coverage at 3 Å spectral resolution.

[1]The STARKLINK Software Group homepage website is http://starlink.jach.hawaii.edu/starlink

[2]PAMELA was written by T. R. Marsh and can be found in the STARKLINK distribution Hawaiki and later releases.

3 ATMOSPHERE AND EVOLUTION MODELS

For all observed targets, we have used spectroscopic and photometric data to determine spectral types by human inspection. We have also derived atmospheric parameters and chemical abundances using the different methods described in this section. Effective temperatures and $\log g$ values can be derived for most white dwarfs using photometric fits (Koester, Schulz & Weidemann 1979; Bergeron, Leggett & Ruiz 2001). For DA and DB stars, an independent method is to determine these parameters from spectroscopic line fits (Bergeron, Saffer & Liebert 1992; Beauchamp et al. 1999). For these spectral types, we refrain from performing simultaneous fits of the photometric and spectroscopic data, which would not improve accuracy because of the known systematic offset between both techniques (Tremblay et al. 2019a). Instead in Section 4, we compare the results of both methods in order to better understand possible model atmosphere systematics and photometric colour calibration issues.

All objects in the Northern hemisphere are also included in the sample discussed in Paper II, where for homogeneity only photometric parameters are employed. In comparison, here we also report on our detailed spectroscopic analysis and describe the properties of 75 additional white dwarf candidates in the Southern hemisphere.

3.1 Photometric parameters

Photometric temperatures, $\log g$ and masses are determined from *Gaia* DR2 photometry and astrometry using the same method as that outlined in Gentile Fusillo et al. (2019). In brief, we rely on our own grids of pure-H, pure-He, and mixed H/He 1D model atmospheres (Tremblay, Bergeron & Gianninas 2011; Cukanovaite et al. 2019) and the mass–radius relation of Fontaine, Brassard & Bergeron (2001) for thick (H-atmospheres) and thin (He-atmospheres) hydrogen layers. The only differences are that we have neglected reddening and adopted grid of model fluxes that correspond to the newly identified atmospheric composition. We also rely on Pan-STARRS photometry when available, resulting in two different sets of atmospheric

parameters using the same model atmospheres and *Gaia* parallaxes. Paper II demonstrates that *Gaia* DR2 and Pan-STARRS are generally in good agreement except for crowded regions of the sky or white dwarfs with close, bright companions.

Bergeron et al. (2019) have demonstrated that pure-He atmospheres result in spuriously high masses and are unable to accurately reproduce the so-called bifurcation in the *Gaia* DR2 HR diagram corresponding to $7000 < T_{\rm eff} < 11\,000$ K (Gaia Collaboration et al. 2018b; Gentile Fusillo et al. 2019). As a consequence, here and in Paper II we now rely on mixed atmospheres with $\log({\rm H/He}) = -5$ in number, which is well below spectroscopic detection limits (Rolland, Bergeron & Fontaine 2018), for all photometric fits of DC white dwarfs above 7000 K. For DC stars within $5000 < T_{\rm eff} < 7000$ K, we use pure-helium atmospheres if we can rule out the presence of the predicted H α line from pure-H model atmospheres. We note that pure-H and pure-He solutions are similar to within a few per cent in this temperature range. Below these temperatures, we assume a pure-hydrogen atmosphere for all DC white dwarfs because it is difficult to constrain the atmospheric composition with optical, near-IR, and mid-IR photometry alone (Gentile Fusillo et al. 2020).

In all cases, we quote the small intrinsic fitting errors and refer to Section 4 for a discussion on extrinsic errors from photometric calibration. Paper II relies on the same set of photometric parameters as described above in their statistical analysis.

For metal-rich DZ, DZA, and DAZ white dwarfs, and similarly for carbon-bearing DQ objects, we use the atmosphere code of Koester (2010) to derive atmospheric parameters and chemical abundances from iterative fits of the photometry, astrometry, and spectroscopy (Hollands, Gänsicke & Koester 2018a; Coutu et al. 2019). This method allows for the non-negligible feedback of metal lines on predicted photometric colours, which determine $T_{\rm eff}$ and $\log g$ values. With these quantities fixed, spectroscopy largely determines the chemical composition. The procedure is iterated until convergence. For a handful of these objects, we postpone a dedicated analysis to future papers (Hollands et al. and Gänsicke et al., in preparation).

3.2 Spectroscopic parameters

We derive $T_{\rm eff}$ and $\log g$ values from spectroscopic fits of non-magnetic DA white dwarfs with *Gaia* temperatures above 6000 K. We rely on the model atmospheres of Tremblay et al. (2011) with 3D corrections from Tremblay et al. (2013). The Balmer line fitting procedure is the same as that reported in Gianninas, Bergeron & Ruiz (2011) and Tremblay et al. (2011). In brief, we first normalize the individual Balmer lines to a continuum set to unity, defined by fitting a model spectrum to the observations where we include a polynomial with of the order of 10 free parameters to account for residual errors in the flux calibration. We then perform a χ^2 minimization between the observed and predicted line profiles, convolved with a Gaussian instrumental profile with a resolution of 2 Å (FWHM). In all cases, we only quote the intrinsic fitting errors. External errors from the flux calibration and fitting procedure are estimated at 0.038 dex in $\log g$ and 1.2 per cent in $T_{\rm eff}$ (Liebert, Bergeron & Holberg 2005).

For DA white dwarfs with temperatures below 6000 K, the lines are too weak for a meaningful determination of the spectroscopic parameters. Therefore, we simply compare observed H α line profiles with predictions using photometric atmospheric parameters to flag any outliers and systematic model effects.

For two DBA white dwarfs, we rely on the 3D model atmospheres of Cukanovaite et al. (2018), Cukanovaite et al. (2019) to constrain the spectroscopic atmospheric parameters and hydrogen abundances with a fitting procedure similar to that of Bergeron et al. (2011).

The spectra of DC and magnetic white dwarfs are not fitted. White dwarf candidates that were found to be main-sequence stars are not analysed further as it is outside of the scope of this paper, although we attempt to explain the reason why they contaminated the initial selection of Gentile Fusillo et al. (2019) in the *Gaia* DR2 HR diagram.

4 RESULTS

From the 230 objects observed, all 191 spectroscopically confirmed white dwarfs have spectral types in Table 2. These objects also have at least one set of either *Gaia* or Pan-STARRS photometric atmospheric parameters (using either pure-H, pure-He, or mixed H/He model atmospheres), and in the case of warmer DA and DBA white dwarfs, an independent set of atmospheric parameters from the analysis of the optical spectrum. The resulting Pan-STARRS photometric distribution of $\log g$ as a function of $T_{\rm eff}$ is shown in Fig. 1. We flag with an asterisk in the WD J name those objects where the parallax value is below 25 mas but for which 40-pc membership is still possible within 1σ. Many of these objects may therefore be excluded from the sample by the upcoming third data release of *Gaia* (DR3).

All white dwarfs with traces of metals or carbon, and for which we have performed a combined fit of photometry and spectroscopy, are also listed in Tables 4 (hydrogen-dominated atmospheres with metals), 6 (helium-dominated atmospheres with metals), and 7 (DQ white dwarfs), where our best estimates of atmospheric parameters and chemical abundances are found. All 39 main-sequence star contaminants are discussed in Section 4.7.

4.1 DA white dwarfs

The spectra for all 89 DA white dwarfs are shown in Figs A1–A4. In most cases, the Balmer lines are too weak for a meaningful fit. However for the subset of 40 objects with *Gaia* $T_{\rm eff} \geq 6000$ K (excluding two He-rich DA white dwarfs), fits are presented in Figs A6–A7, with best-fitting atmospheric parameters corrected for 3D convection (Tremblay et al. 2013) identified in Table 2. *Gaia* photometric temperatures are systematically lower by 2.4 per cent compared to the spectroscopic values, an offset very similar to that previously identified in Tremblay et al. (2019a) and Genest-Beaulieu & Bergeron (2019) from larger spectroscopic samples. Results with Pan-STARRS are very similar, with photometric temperatures systematically lower by 2.2 per cent (excluding two hot white dwarfs in crowded fields). Considering external errors on spectroscopic fits (Liebert et al. 2005), in the majority of individual cases the spectroscopic and photometric solutions agree within 2σ. For a number of cool objects with $T_{\rm eff} < 7000$ K, the spectroscopic parameters are likely reliable but with a precision well-below the photometric parameters.

For all objects with *Gaia* $T_{\rm eff} < 6000$ K, in Figs A8–A11 we compare instead the H α line profile with the prediction from the best *Gaia* photometric fit identified in Table 2. In doing so, we have identified a systematic shift where predicted H α equivalent widths (or line strengths) are systematically too small compared to the observed lines. In other words, *Gaia* colours are systematically too red resulting in temperatures that are too low by 2.7 per cent. Pan-STARRS is only marginally better and predicted temperatures are still too low by 1.8 per cent. Neutral broadening dominates in cool DA stars (Tremblay et al. 2010) and the predicted equivalent width of H α depends on $T_{\rm eff}$ and $\log g$, but the influence of non-ideal gas effects is very weak.

Table 2. Spectral types and parameters of the white dwarf sample.

WD J name	SpT	$T_{\rm eff}$ (K) 3D spectro	log g 3D spectro	$T_{\rm eff}$ (K) *Gaia*	log g *Gaia*	$T_{\rm eff}$ Pan-STARRS	log g Pan-STARRS	Note
001324.45+543757.64	DC	–	–	–	–	4070 (20)	7.75 (0.02)	
001333.22−021319.42	DC	–	–	4440 (90)	7.80 (0.07)	4590 (30)	7.90 (0.03)	
002116.21+253134.45	DA	9680 (50)	8.62 (0.04)	9190 (170)	8.49 (0.04)	–	–	
002450.37+683446.85	DC	–	–	5520 (70)	8.20 (0.04)	5390 (20)	8.10 (0.02)	
002702.93+055433.40	DC	–	–	5050 (70)	8.28 (0.06)	5260 (20)	8.39 (0.02)	
003047.74+034657.93	DC	–	–	6390 (30)	8.07 (0.02)	6340 (40)	8.04 (0.04)	
005503.58+101005.56	DA	6160 (100)	7.60 (0.24)	6190 (30)	8.02 (0.02)	6230 (10)	8.03 (0.01)	
010338.56−052251.96	DAH	–	–	8960 (180)	9.34 (0.03)	8750 (70)	9.31 (0.01)	
010416.07−035025.39	DA	–	–	5280 (70)	8.29 (0.05)	5310 (20)	8.31 (0.02)	
012923.99+510846.97	DA	22550 (90)	8.01 (0.01)	21850 (270)	8.00 (0.02)	–	–	(a)
013055.01+441423.29	DZA	–	–	4990 (40)	7.99 (0.04)	5000 (20)	7.97 (0.02)	
013705.08−020738.75	DA	7570 (40)	8.35 (0.06)	7260 (80)	8.31 (0.03)	7330 (40)	8.33 (0.02)	
014258.08+073045.39	DA	–	–	5500 (70)	8.01 (0.05)	5560 (20)	8.04 (0.02)	
015825.83+253051.31	DC	–	–	–	–	4220 (20)	7.77 (0.03)	
020210.60+160203.31	DZ	–	–	4760 (70)	8.13 (0.05)	4930 (20)	8.24 (0.02)	
020809.31+372939.12	DA	–	–	5560 (50)	8.50 (0.03)	5700 (25)	8.55 (0.02)	
021839.49+501351.28	DA	–	–	4840 (30)	7.76 (0.02)	4900 (20)	7.80 (0.01)	
022111.49+533330.39	DC	–	–	6630 (50)	8.15 (0.03)	6050 (40)	7.90 (0.01)	
022157.89+044517.91	DA	7520 (100)	8.24 (0.15)	7150 (100)	8.06 (0.04)	7270 (20)	8.09 (0.01)	
022704.24+591502.04	DA	7330 (40)	7.75 (0.06)	7290 (50)	7.85 (0.02)	7250 (40)	7.84 (0.02)	
022724.62+180724.03	DA	8800 (20)	8.03 (0.03)	8440 (90)	7.97 (0.05)	8530 (60)	8.00 (0.04)	
023117.04+285939.88	DA	7200 (20)	7.97 (0.03)	6980 (30)	7.67 (0.02)	6920 (10)	7.65 (0.02)	(b)
025007.11+081753.42	DC	–	–	4330 (90)	7.65 (0.08)	4550 (30)	7.80 (0.02)	
025328.32+375959.38	DA	6550 (60)	7.70 (0.12)	6480 (40)	7.92 (0.03)	6600 (40)	7.97 (0.02)	
030350.56+060748.75	DXP	–	–	20050 (7000)	8.94 (0.30)	–	–	(c)
030850.43+512822.32	DA	–	–	5090 (40)	7.92 (0.04)	5210 (20)	8.00 (0.02)	
031124.57−085324.98	DA	–	–	4920 (60)	7.79 (0.05)	5060 (20)	7.89 (0.03)	
031138.80−055117.55	DC	–	–	–	–	4220 (10)	7.83 (0.01)	
031907.61+423045.45	DC	–	–	11020 (80)	8.23 (0.02)	10880 (60)	8.22 (0.01)	
032631.46+155714.79	DA	–	–	5680 (70)	8.18 (0.05)	5760 (20)	8.22 (0.02)	
034501.53−034849.73	DC	–	–	–	–	4390 (20)	7.87 (0.02)	(d)
034501.70−034844.85	DA	–	–	4960 (50)	7.85 (0.05)	5030 (10)	7.89 (0.02)	(d)
034511.83+194026.08	DA	12780 (70)	8.17 (0.02)	12450 (100)	8.23 (0.01)	12430 (80)	8.23 (0.01)	
035556.50+452510.26	DA	–	–	5060 (30)	7.91 (0.03)	5130 (20)	7.95 (0.02)	
035826.49+215726.16	DAZ	–	–	6660 (30)	8.17 (0.02)	6770 (30)	8.22 (0.01)	
040242.39+152742.47	DC	–	–	6850 (30)	8.14 (0.02)	6910 (30)	8.16 (0.02)	
041246.85+754942.26	DA(e)	–	–	8510 (90)	8.25 (0.02)	8380 (50)	8.22 (0.01)	
042313.75+574526.76	DC	–	–	7110 (40)	8.18 (0.02)	7170 (40)	8.21 (0.01)	
042731.73−070802.80	DC	–	–	6850 (40)	8.15 (0.02)	7050 (40)	8.21 (0.02)	
∗ 052400.25−060402.72	DC	–	–	6620 (110)	8.25 (0.05)	–	–	
052436.27−053510.52	DA	17510 (80)	8.02 (0.02)	17300 (130)	8.03 (0.01)	16410 (150)	7.97 (0.01)	
052913.45+430025.89	DQ	–	–	8880 (80)	8.05 (0.02)	8740 (60)	8.03 (0.02)	
053026.01+393917.04	DA	–	–	5450 (50)	7.92 (0.04)	5440 (20)	7.92 (0.02)	
053714.90+675950.51	DAH	–	–	7750 (40)	8.33 (0.01)	7740 (30)	8.33 (0.01)	(e)
053916.45+435234.70	DC	–	–	5910 (50)	8.14 (0.03)	5900 (20)	8.14 (0.02)	
054839.48+132551.76	DC	–	–	–	–	4110 (60)	7.86 (0.05)	
∗ 055231.03+164250.27	DBA	–	–	11950 (90)	8.17 (0.02)	–	–	
055443.04−103521.34	DZ	–	–	6570 (20)	8.17 (0.01)	6600 (20)	8.19 (0.01)	
061848.64+620425.54	DC	–	–	4530 (50)	7.80 (0.04)	4670 (30)	7.90 (0.03)	
062006.01+420544.38	DA	–	–	6650 (70)	8.33 (0.03)	6580 (30)	8.31 (0.03)	(f)
063235.80+555903.12	DAH	–	–	9970 (80)	8.52 (0.02)	9840 (40)	8.50 (0.01)	
063931.88+243546.15	DC	–	–	8480 (110)	7.92 (0.04)	–	–	
064111.93−043212.31	DC	–	–	–	–	4130 (20)	7.80 (0.01)	
064400.61+092605.76	DAH	–	–	6080 (50)	8.05 (0.03)	6140 (30)	8.08 (0.02)	
064926.55+752124.97	DAH	–	–	6440 (40)	8.21 (0.02)	6500 (30)	8.23 (0.01)	(g)
065729.40+055047.87	DC	–	–	6020 (60)	8.21 (0.04)	6090 (30)	8.24 (0.02)	
065845.23−011552.84	DA	–	–	4840 (90)	8.02 (0.08)	4890 (30)	8.05 (0.03)	
065910.86+122526.52	DA	–	–	4920 (60)	7.85 (0.05)	5040 (10)	7.93 (0.02)	
070356.98+780504.72	DA	–	–	5340 (20)	7.86 (0.02)	5400 (10)	7.89 (0.01)	
070357.43+253418.34	DBA	11710 (180)	8.01 (0.14)	11500 (100)	7.97 (0.02)	11190 (50)	7.93 (0.01)	
070549.32+514250.52	DA	–	–	4970 (90)	8.14 (0.08)	5070 (20)	8.19 (0.02)	

Table 2 – *continued*

WD J name	SpT	$T_{\rm eff}$ (K) 3D spectro	log g 3D spectro	$T_{\rm eff}$ (K) *Gaia*	log g *Gaia*	$T_{\rm eff}$ Pan-STARRS	log g Pan-STARRS	Note
071206.15−042815.30	DA	–	–	5280 (60)	8.06 (0.04)	5390 (20)	8.13 (0.02)	
071703.10+112541.55	DA	–	–	4690 (40)	7.78 (0.03)	4800 (20)	7.85 (0.02)	
072205.61+280626.98	DA	–	–	5200 (70)	8.03 (0.06)	5220 (20)	8.04 (0.02)	
072300.22+161703.98	DA	11760 (80)	8.29 (0.02)	11580 (140)	8.31 (0.02)	11610 (110)	8.33 (0.01)	
072434.96−133828.38	DA	–	–	4940 (50)	8.04 (0.05)	5030 (70)	8.10 (0.05)	
073024.53+533211.95	DC	–	–	4530 (60)	7.86 (0.06)	4740 (30)	8.01 (0.03)	
075252.85−030707.97	DC	–	–	–	–	4470 (40)	7.79 (0.03)	
∗ 080247.02+564640.62	DC	–	–	4320 (50)	7.80 (0.06)	–	–	
081325.13+195729.18	DC	–	–	–	–	4010 (30)	7.79 (0.03)	
082532.35−072823.21	DA	15560 (110)	7.97 (0.02)	15550 (90)	7.97 (0.01)	14750 (170)	7.91 (0.01)	
083150.62−164329.97	DC	–	–	–	–	4220 (40)	7.93 (0.04)	
084515.55+611705.79	DA	–	–	5470 (30)	8.02 (0.02)	5540 (20)	8.05 (0.02)	(d)
084516.87+611704.81	DAH	–	–	5820 (40)	8.09 (0.02)	5850 (20)	8.09 (0.01)	(d)
084957.48−015612.38	DC	–	–	4820 (20)	7.89 (0.02)	4880 (10)	7.93 (0.01)	
085534.72−083345.34	DC	–	–	4500 (60)	7.75 (0.06)	4640 (10)	7.85 (0.02)	
085804.42+681338.66	DC	–	–	4580 (60)	7.94 (0.06)	4630 (10)	7.98 (0.02)	
090912.98−224625.86	DC	–	–	4510 (100)	7.98 (0.09)	4570 (40)	8.01 (0.04)	
091353.95+620601.69	DA	–	–	5650 (30)	8.06 (0.02)	5740 (20)	8.10 (0.01)	
092542.84+612012.85	DA	8200 (140)	8.65 (0.17)	8010 (30)	7.85 (0.01)	7950 (30)	7.84 (0.01)	(i)
093948.69−145836.69	DC	–	–	–	–	4170 (20)	7.83 (0.02)	
095447.49+670208.00	DA	–	–	5700 (20)	8.20 (0.01)	5700 (20)	8.20 (0.01)	
100424.18−050614.92	DC	–	–	–	–	4160 (20)	7.81 (0.02)	(j)
∗ 102203.66+824310.00	DA	–	–	5490 (70)	8.32 (0.04)	–	–	
103055.44−142400.53	DA	5980 (80)	7.89 (0.19)	6040 (50)	8.21 (0.03)	5990 (20)	8.18 (0.01)	
111913.56−083137.22	DA	–	–	5530 (30)	8.04 (0.02)	5590 (20)	8.06 (0.02)	
113444.64+610826.68	DAZ	7610 (50)	8.03 (0.08)	7440 (40)	7.95 (0.01)	7510 (20)	7.98 (0.01)	
113840.67−131338.55	DC	–	–	5940 (20)	8.15 (0.01)	6020 (30)	8.17 (0.02)	
120055.89−103220.61	DA	8070 (60)	8.40 (0.08)	7950 (50)	8.44 (0.02)	8010 (30)	8.46 (0.01)	
121701.84+684851.45	DA	6440 (110)	8.25 (0.20)	6420 (40)	8.38 (0.02)	6400 (60)	8.37 (0.02)	(k)
122956.02−070727.57	DA	–	–	4950 (40)	7.80 (0.03)	5000 (20)	7.82 (0.02)	
124828.17−102857.82	DC	–	–	7130 (70)	8.27 (0.03)	7120 (30)	8.27 (0.01)	
130503.44+702243.05	DC	–	–	4860 (280)	8.99 (0.14)	5060 (170)	9.06 (0.07)	
135509.42−262248.95	DA	5922 (120)	7.72 (0.25)	6080 (40)	8.06 (0.02)	6050 (30)	8.05 (0.01)	
∗ 140841.83−264948.55	DC	–	–	7120 (90)	8.35 (0.04)	–	–	
144318.17−143715.32	DA	6570 (60)	7.88 (0.11)	6610 (50)	8.20 (0.02)	6650 (40)	8.21 (0.02)	(a)
144528.12+292124.29	DA	–	–	5350 (20)	7.94 (0.02)	5450 (20)	7.99 (0.02)	
151534.80+823028.99	DZH	–	–	4360 (80)	7.80 (0.06)	4540 (80)	7.92 (0.06)	
160041.14−165430.24	DC	–	–	–	–	4460 (80)	8.13 (0.06)	
160415.07−072658.01	DC	–	–	4770 (60)	8.47 (0.04)	4710 (40)	8.38 (0.02)	
160420.47−133123.84	DA	–	–	4960 (40)	7.76 (0.04)	5020 (20)	7.78 (0.01)	
160606.17+702226.94	DA	–	–	6290 (40)	7.97 (0.02)	6290 (40)	7.96 (0.03)	(a)
160700.89−140423.88	DAH	–	–	5700 (30)	8.05 (0.02)	5710 (30)	8.02 (0.02)	
161330.58+442754.13	DA	–	–	5280 (140)	8.00 (0.10)	–	–	
161916.31−183114.19	DA	–	–	5340 (90)	8.34 (0.06)	5410 (20)	8.40 (0.02)	
162125.64−055219.84	DC	–	–	4570 (70)	7.74 (0.06)	4710 (20)	7.83 (0.03)	
162818.90−173917.89	DA	–	–	4820 (40)	7.79 (0.03)	4890 (20)	7.83 (0.02)	
164951.45−215503.96	DA	–	–	5040 (40)	7.94 (0.04)	5090 (20)	7.98 (0.02)	
170438.32−144620.79	DA	7520 (40)	8.50 (0.06)	7440 (100)	8.42 (0.03)	7340 (30)	8.40 (0.01)	
170502.87−014502.70	DC	–	–	4730 (40)	7.97 (0.03)	4740 (10)	7.98 (0.01)	
170552.58+260551.20	DA	–	–	5950 (40)	8.20 (0.02)	6040 (30)	8.24 (0.02)	(l)
171620.72−082118.60	DQ	–	–	6000 (90)	7.86 (0.05)	6120 (20)	7.92 (0.02)	
172006.79+102227.98	DC	–	–	4940 (60)	7.90 (0.05)	5050 (20)	7.98 (0.02)	
172945.19+143541.28	DC	–	–	4730 (50)	8.25 (0.04)	4840 (20)	8.31 (0.02)	
173337.18+290338.04	DC	–	–	6340 (40)	8.15 (0.02)	6370 (20)	8.16 (0.01)	
173404.42+442303.09	DA	–	–	5000 (60)	7.99 (0.05)	5140 (20)	8.07 (0.02)	
174620.41−123425.48	DA	–	–	5970 (70)	8.24 (0.04)	6160 (30)	8.33 (0.02)	
174935.61−235500.63	DAZ	7200 (30)	7.75 (0.06)	7000 (50)	7.87 (0.02)	7420 (40)	8.06 (0.01)	
175352.16+330622.62	DA	17480 (80)	8.06 (0.01)	17120 (110)	7.99 (0.01)	17160 (150)	8.00 (0.01)	
175919.66+392504.95	DC	–	–	4540 (70)	7.82 (0.05)	4580 (20)	7.84 (0.02)	
∗ 180218.60+135405.46	DAZ	8570 (30)	8.39 (0.05)	8310 (110)	8.09 (0.04)	–	–	
180919.46+295720.85	DA	23280 (70)	8.40 (0.01)	22515 (160)	8.39 (0.01)	–	–	(a)
181539.13−114041.83	DC	–	–	4830 (70)	7.86 (0.06)	4855 (20)	7.88 (0.02)	
181745.57−133531.54	DA	6290 (220)	8.76 (0.36)	6050 (70)	8.38 (0.03)	5930 (40)	8.33 (0.02)	

Table 2 – *continued*

WD J name	SpT	$T_{\rm eff}$ (K) 3D spectro	log g 3D spectro	$T_{\rm eff}$ (K) *Gaia*	log g *Gaia*	$T_{\rm eff}$ Pan-STARRS	log g Pan-STARRS	Note
181909.96−193438.00	DC	–	–	–	–	4500 (30)	7.87 (0.03)	
182021.81+261936.58	DA	–	–	4890 (70)	8.19 (0.06)	5000 (20)	8.24 (0.02)	
182147.11+550906.70	DA	–	–	4890 (60)	7.86 (0.05)	4870 (50)	7.85 (0.04)	
182347.60−112347.38	DA	–	–	5560 (110)	8.01 (0.07)	5850 (30)	8.18 (0.02)	
182359.62+202248.81	DC	–	–	4950 (40)	8.01 (0.04)	4920 (20)	7.98 (0.02)	
182417.72+120945.86	DA	–	–	5160 (70)	8.05 (0.05)	5170 (20)	8.06 (0.01)	
182458.45+121316.82	DZ	–	–	–	–	4330 (31)	7.92 (0.04)	
182524.24+113557.34	DA	–	–	4850 (30)	7.87 (0.02)	4900 (10)	7.91 (0.01)	
182624.44+112049.58	DA	–	–	4860 (50)	7.85 (0.04)	4850 (10)	7.80 (0.01)	
182951.89−053623.17	DA	–	–	5450 (60)	7.97 (0.04)	5480 (30)	8.00 (0.02)	(d)
182952.07−053622.88	DC	–	–	6490 (80)	8.07 (0.04)	6300 (30)	7.99 (0.03)	(d)
183158.72+465828.98	DA	7650 (20)	8.11 (0.03)	7380 (30)	8.02 (0.01)	7380 (30)	8.02 (0.01)	
183518.23+642117.68	DC	–	–	4860 (30)	7.99 (0.04)	4870 (20)	7.99 (0.02)	
183352.68+321757.25	DZA	–	–	7540 (100)	7.88 (0.04)	8240 (50)	8.09 (0.02)	
∗ 184733.18+282057.54	DC	–	–	4630 (70)	8.14 (0.07)	–	–	
184741.53+122631.75	DA	10450 (30)	8.42 (0.02)	10020 (150)	8.40 (0.03)	–	–	
184907.50−073619.82	DC	–	–	6190 (110)	8.15 (0.06)	6300 (20)	8.22 (0.02)	
185517.99+535923.18	DC	–	–	4610 (50)	7.88 (0.04)	4670 (10)	7.93 (0.01)	
191246.12+024239.11	DZ	–	–	6280 (40)	8.11 (0.02)	7050 (50)	8.40 (0.02)	
192126.76+061322.71	DA	–	–	5880 (20)	8.14 (0.01)	5960 (10)	8.19 (0.01)	
∗ 192206.20+023313.29	DZ	–	–	5800 (390)	9.10 (0.02)	–	–	
192359.24+214103.62	DA	9280 (20)	8.06 (0.02)	8750 (50)	7.55 (0.02)	8840 (40)	7.58 (0.02)	(b)
192626.93+462015.10	DA	8170 (30)	8.30 (0.04)	8130 (50)	8.21 (0.02)	8020 (30)	8.19 (0.02)	
192724.75+564455.34	DA	6750 (70)	8.45 (0.12)	6530 (60)	8.36 (0.02)	6550 (20)	8.36 (0.01)	
192938.65+111752.41	DA	21130 (90)	8.00 (0.01)	20220 (300)	7.94 (0.02)	16550 (370)	7.75 (0.03)	
193019.71−005730.56	DC	–	–	7620 (80)	8.17 (0.03)	7580 (30)	8.16 (0.01)	
∗ 193500.68−172443.11	DC	–	–	4480 (60)	8.17 (0.02)	–	–	
193618.58+263255.79	DA	25220 (90)	8.54 (0.01)	24380 (170)	8.53 (0.01)	19270 (300)	8.34 (0.02)	(m)
193955.83+661856.08	DC	–	–	5070 (40)	8.14 (0.03)	5220 (20)	8.22 (0.02)	(k)
195003.62+003357.09	DA	–	–	5800 (40)	7.93 (0.03)	5820 (20)	7.94 (0.01)	
195119.15+420941.40	DA	–	–	5050 (50)	8.02 (0.05)	5050 (20)	8.02 (0.02)	
195151.76+402629.07	DC	–	–	5050 (80)	8.22 (0.06)	5140 (30)	8.29 (0.02)	
200445.49+010929.21	DA	6770 (60)	8.30 (0.10)	6510 (70)	8.32 (0.03)	–	–	
200632.25−210142.90	DA	–	–	5070 (60)	7.90 (0.05)	5110 (20)	7.93 (0.02)	
200850.81−161943.62	DC	–	–	5470 (70)	8.28 (0.04)	5530 (20)	8.31 (0.02)	
201216.01−221023.03	DC	–	–	5500 (70)	8.12 (0.04)	5520 (10)	8.13 (0.01)	
201530.35+000111.80	DC	–	–	4760 (40)	7.92 (0.03)	4900 (20)	8.03 (0.02)	
202157.83+545438.25	DC	–	–	5940 (60)	8.18 (0.03)	5940 (30)	8.19 (0.02)	
203100.56−145041.38	DC	–	–	4460 (90)	8.03 (0.08)	4560 (20)	8.06 (0.03)	
203102.15+393454.05	DC	–	–	4530 (70)	7.87 (0.06)	4640 (20)	7.93 (0.03)	
203321.86+395409.76	DA	–	–	5930 (20)	8.40 (0.01)	5890 (20)	8.37 (0.01)	
204832.02+511047.25	DC	–	–	4840 (80)	7.92 (0.07)	4860 (20)	7.94 (0.02)	
210646.77+010635.24	DA	6250 (120)	8.15 (0.22)	6030 (40)	7.94 (0.03)	6060 (20)	7.96 (0.02)	
210854.87−031202.98	DC	–	–	5230 (50)	7.93 (0.04)	5390 (20)	8.04 (0.02)	
213343.70+241457.72	DA	6650 (80)	8.53 (0.14)	6320 (40)	8.40 (0.02)	6350 (30)	8.39 (0.01)	
213517.95+463318.21	DA	–	–	4900 (100)	7.92 (0.09)	4790 (30)	7.81 (0.02)	(l)
213957.13−124549.09	DA	7780 (40)	8.25 (0.06)	7730 (160)	8.36 (0.05)	7850 (180)	8.39 (0.05)	
215008.33−043900.36	DC	–	–	5320 (80)	8.32 (0.06)	5450 (30)	8.39 (0.03)	
215140.11+591734.85	DAH	–	–	5100 (10)	7.98 (0.01)	5130 (10)	8.01 (0.01)	(n)
215759.55+270519.13	DC	–	–	4500 (60)	7.73 (0.05)	4580 (20)	7.77 (0.02)	
215839.14−023916.44	DC	–	–	4780 (40)	7.84 (0.03)	4920 (10)	7.94 (0.02)	(d)
215847.13−024024.42	DC	–	–	4730 (50)	7.83 (0.04)	4820 (10)	7.90 (0.02)	(d)
220052.62+582202.29	DA	–	–	5380 (50)	7.94 (0.04)	5500 (30)	8.01 (0.02)	
220253.65+023741.53	DA	–	–	5750 (50)	8.20 (0.04)	5770 (20)	8.20 (0.02)	
220751.81+342845.79	DA	10190 (30)	8.05 (0.03)	10070 (40)	8.01 (0.01)	9990 (20)	8.00 (0.01)	
221800.59+560214.92	DC	–	–	–	–	4440 (20)	7.73 (0.02)	
222547.07+635727.37	DC	–	–	5030 (50)	7.81 (0.03)	5103 (20)	7.88 (0.02)	
223059.16+225454.09	DC	–	–	5720 (30)	8.20 (0.02)	5740 (20)	8.20 (0.01)	
223418.83+145654.42	DA	6380 (60)	7.96 (0.12)	6290 (50)	8.02 (0.03)	6280 (20)	8.01 (0.01)	
225257.98+392817.40	DC	–	–	4830 (50)	7.94 (0.05)	4900 (20)	7.99 (0.02)	
225338.11+813039.98	DC	–	–	5300 (80)	8.15 (0.06)	–	–	(o)

Table 2 – *continued*

WD J name	SpT	$T_{\rm eff}$ (K) 3D spectro	log g 3D spectro	$T_{\rm eff}$ (K) *Gaia*	log g *Gaia*	$T_{\rm eff}$ Pan-STARRS	log g Pan-STARRS	Note
225725.27+513008.56	DA	7260 (50)	8.30 (0.07)	7210 (310)	8.41 (0.10)	7350 (50)	8.44 (0.02)	
230056.46+640815.95	DC	–	–	4530 (70)	7.85 (0.06)	4590 (20)	7.90 (0.02)	
230303.62+463241.98	DC	–	–	4580 (70)	8.05 (0.06)	4680 (30)	8.12 (0.03)	
230550.09+392232.88	DC	–	–	6550 (120)	8.88 (0.04)	7030 (60)	9.01 (0.02)	
231726.74+183052.75	DZ	–	–	4600 (220)	8.78 (0.13)	4640 (40)	8.77 (0.04)	
∗ 235750.73+194905.90	DZ	–	–	5810 (50)	7.89 (0.04)	–	–	

(a) also in Scholz et al. (2018), (b) double degenerate candidate, (c) also in Landstreet & Bagnulo (2020), (d) wide double white dwarf, (e) DAH: in Limoges et al. (2015), (f) likely He-rich white dwarf, (g) DA in Limoges et al. (2015), (h) D: in Leggett et al. (2018), (i) FAST spectrum has poor S/N, Balmer line fit uncertain, (j) main-sequence star in Reid et al. (2004), (k) WD in Greenstein (1984), (l) DC in Oswalt & Strunk (1994), (m) DA in Motch et al. (1998), (n) also in Landstreet & Bagnulo (2019), (o) DC: in Limoges et al. (2015). Objects with an asterisk before their name have a parallax value outside of 40 pc, but may still be within that volume at 1σ. For all photometric fits, we have used either pure-H (DA, DAZ, DAH, and DC coooler than 5000 K), pure-He (He-rich DA and DC in the range 5000 $< T_{\rm eff} <$ 7000 K), or mixed log(H/He) $= -5$ model atmospheres (DZ, DZH, DZA, DQ, DBA, and DC warmer than 7000 K). All quoted uncertainties represent the intrinsic fitting errors.

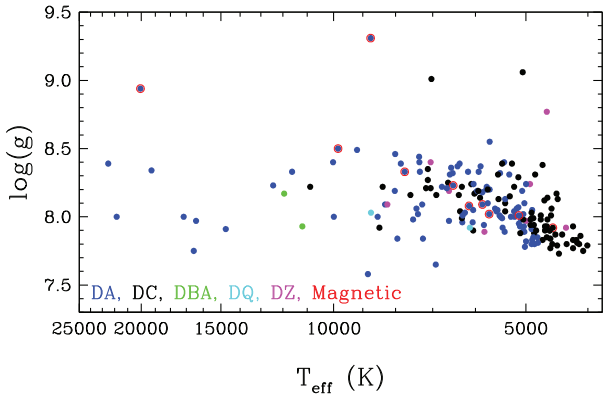

Figure 1. log g versus effective temperature distribution for 191 confirmed white dwarfs within 40 pc based on Pan-STARRS photometric parameters. For 19 objects with missing or unreliable Pan-STARRS photometry, we relied on *Gaia* parameters instead. The ultra-cool DZ WD J1922+0233 does not have reliable atmospheric parameters and is omitted from the figure. Spectral types are colour coded for DA (blue), DC (black), DBA (green), DQ (cyan), and DZ (magenta) white dwarfs. Magnetic stellar remnants have red contours.

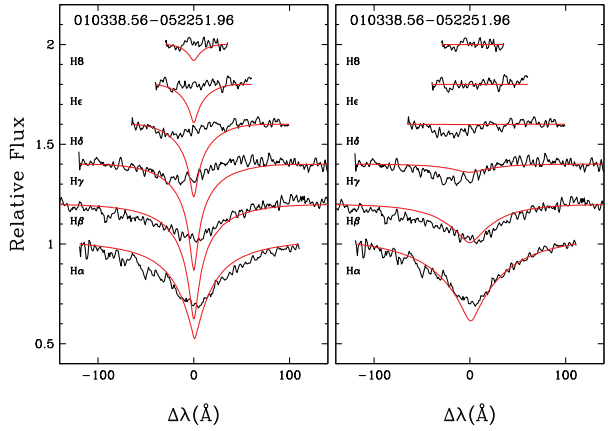

Figure 2. Left-hand panel: Comparison of the normalized observed Balmer line profiles for WD J0103−0522 with a DA model atmosphere at the *Gaia* derived photometric parameters ($T_{\rm eff}$ = 8960 K and log g = 9.34). Right-hand panel: Fit of the observations using He-rich model atmospheres with log(H/He) = −1.70. The resulting best-fitting parameters ($T_{\rm eff}$ = 8520 K and log g = 9.06), excluding the constraint from parallax, should be taken with caution given the relatively poor quality of the fit and we consider the photometric parameters more reliable.

The offset between observed and predicted H α is of very similar amplitude and in the same direction as the issue identified above between photometric temperatures and spectroscopic temperatures from Balmer line fits of warmer DA white dwarfs, where Stark broadening dominates. This raises doubts that issues with the current implementation of Stark broadening theory (Tremblay & Bergeron 2009) are the source of the offset for hotter DA white dwarfs, as there would be no reason for the similar observed pattern at cool temperatures. Furthermore, there is no clear evidence of an offset between predicted and observed *Gaia* or Pan-STARRS absolute magnitudes in warm DA white dwarfs (Tremblay et al. 2019a), suggesting that the issue is with observed colours rather than a constant shift in photometric zero points. A possible explanation is that the photometric colour calibration of *Gaia* and Pan-STARRS is the source of the offset (Maíz Apellániz & Weiler 2018) and that the hot DA white dwarf spectroscopic temperature scale remains adequate (Narayan et al. 2019; Gentile Fusillo et al. 2020). In Figs A8–A11, we have corrected the *Gaia* $T_{\rm eff}$ values by +2.7 per cent to demonstrate the good agreement with observed spectroscopy and to flag outliers. We now discuss peculiar DA stars in turn.

WD J0103−0522 is one of the most massive known white dwarfs with a photometric log g = 9.34 ± 0.03, corresponding to a mass of 1.31 ± 0.01 $M_\odot$. Within 40 pc, only the previously known pure-hydrogen atmosphere DA star WD 2349−031 has a larger mass based on *Gaia* photometry (Gentile Fusillo et al. 2019). In comparison, Balmer lines are clearly detected in WD J0103−0522 but have an unusual asymmetric profile with line centres shifted towards the blue (Fig. 2). Each member of the Balmer series corresponding to a transition to upper level n is progressively more blue-shifted compared to the line that precedes with a transition to the level n − 1, which is inconsistent with a large radial velocity. Furthermore the lines are much broader and shallower than expected for a pure-hydrogen white dwarf at the *Gaia* temperature of 8960 ± 180 K. The object is strikingly similar to PG 1157+004 ($T_{\rm eff}$ = 9425 ± 50 K and log g = 8.66 ± 0.01; Gentile Fusillo et al. 2019) from fig. 17 of Limoges et al. (2015), also a member of the 40-pc sample. These authors had flagged the star as a double degenerate candidate, but given that both PG 1157+004 and WD J0103−0522 are very massive, this appears unlikely. Another possibility is that the atmosphere is a mixture of helium and hydrogen, and that neutral helium broadening in the dense atmosphere is responsible for disrupting the line profiles. Fig. 2 (right-hand panel) demonstrates that a helium-

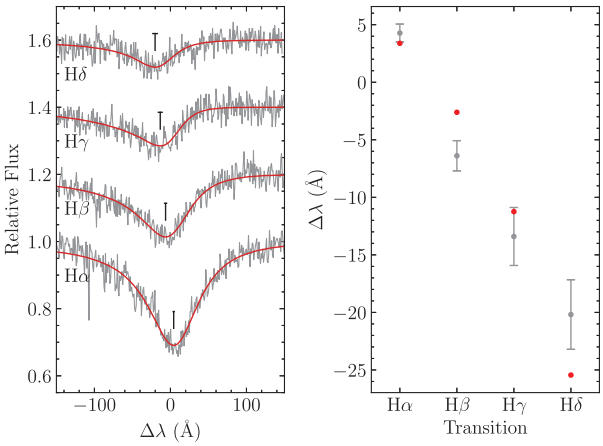

Figure 3. Left-hand panel: Asymmetric-Lorentzian profile fits to Hα–Hδ for WD J0103−0522. The black T symbols mark the position of the best fit to the profile minimum, with their widths indicating the 1σ uncertainties. Right-hand panel: The measured values of the profile minima, fitted with a redshift of 261 ± 40 km s^{-1}, and field strength of 4.8 ± 0.4 MG (red points).

dominated atmosphere with log(H/He) ≈ −1.70 best reproduces the lower Balmer line equivalent widths at the *Gaia* temperature, but is still a rather poor fit to the line asymmetries, wavelength shifts, and Balmer line decrement.

The presence of a magnetic field is common (25–50 per cent) for *Gaia* white dwarfs with >1 M$_\odot$ (see the SDSS-*Gaia* catalogue of Gentile Fusillo et al. 2019). One possibility is that stellar magnetism is responsible for the unusual line shapes. While we do not observe Zeeman splitting, the asymmetry and shifts of the Balmer series can be explained as quadratic Zeeman effect of the π-component. The absence of σ-components can arise from a complex field geometry that leaves them washed out: for example, an offset-dipole configuration where the offset is towards the observer, resulting in a broad distribution of field strengths across the visible hemisphere of the star.

To investigate this possibility, we considered that the quadratic Zeeman shift of each atomic energy level has an n^4 dependence, where n is the principle quantum number. This implies that each member of the Balmer series will be progressively more blue-shifted than the one that precedes it (as appears to be the case in Fig. 2).

While we stop short of a full analysis of the field geometry, we show that the flux minimum of each Balmer line (Hα–Hδ) follows the expected pattern of wavelength shifts. For the purpose of constraining the location of the Balmer line centres, λ_0, we fit each with an asymmetric Lorentzian profile

$$L(\lambda,\lambda_0) = \exp\left(-A\left[1+\left(\frac{\lambda-\lambda_0}{\Gamma(\lambda,\lambda_0)}\right)^2\right]^{-1}\right), \quad (1)$$

where A is fit parameter scaling the line depth, and

$$\Gamma(\lambda,\lambda_0) = a\left[1+\tanh(b(\lambda-\lambda_0))\right], \quad (2)$$

where a and b are fit parameters that control the profile asymmetry. Note that the use of (1 + tanh) acts to keep $\Gamma(\lambda,\lambda_0)$ positive, but bounded for all values of λ. Additionally, this formulation ensures that the minimum is located at λ_0. Continuum normalization was performed by fitting a quadratic polynomial. The resulting fits to the first four Balmer lines are shown in Fig. 3, left-hand panel. The minima (in vacuum wavelengths) for Hα–Hδ were found to be 6568.9 ± 0.8, 4856.3 ± 1.3, 4328.3 ± 2.5, and 4082.7 ± 3.0 Å, respectively.

Table 3. Results from fitting the line shifts of WD J0103−0522 for the different sub components of the Hα–Hδ π-components.

	m	Redshift (km s^{-1})	B (MG)
$2S \rightarrow nP$	0	277 ± 39	5.35 ± 0.25
$2P \rightarrow n(S/D)$	0	271 ± 39	5.04 ± 0.24
$2P \rightarrow nD$	±1	251 ± 38	4.59 ± 0.22
Mean		261 ± 40	4.82 ± 0.37

It is reasonable to assume that the four minima correspond to approximately the same field strength, from the distribution of fields on the visible hemisphere of the star. We therefore fitted the shifts according to those expected from the quadratic Zeeman effect with a single field strength and a redshift as free parameters. We used the shifts as given in Hamada (1971), for transitions of the type $2S \rightarrow nP$ and $2P \rightarrow n(S/D)$, i.e.

$$\Delta k(2S, nP) = 4.96\times10^{-3}B^2(n^4-n^2-28), \quad (3)$$

and

$$\Delta k(2Pm, nlm) = 2.37\times10^{-4}B^2\left[(5n^4-17n^2)(5+m^2) - 252(1+m^2)\right], \quad (4)$$

where Δk is the wavenumber shift in cm^{-1} and m is the magnetic quantum number. Since we are only interested in transitions belonging to the π-component, we have set $m_{\rm up} = 0$ in equation (3), and $m = m_{\rm lo} = m_{\rm hi}$ in equation (4). The resulting fit for the $2S \rightarrow nP$ transitions are given in Fig. 3, right-hand panel, demonstrating good agreement with the quadratic Zeeman effect, and thus providing moderate evidence that WD J0103−0522 is magnetic. The fits to the $2P \rightarrow n(S/D)$ transitions showed similarly good fits, though with some variance between the redshift and field strength parameters. We therefore averaged the parameters across the set of fits, weighted by their respective oscillator strengths (f_{ik} values), which are shown individually and with the mean in Table 3.

At first glance the redshift appears to be extremely large, however, the ultra-massive nature of WD J0103−0522 indicates a gravitational redshift of ≃210 km s^{-1}, implying a radial velocity of 50 ± 40 km s^{-1}. This is consistent with the moderate tangential velocity of 24.20 km s^{-1} from *Gaia* DR2. The magnetic field of 4.82 ± 0.37 MG, can not be taken as representative of the global magnetic field. More likely, it corresponds to the weakest end of the field strength distribution on the stars visible hemisphere, with the higher field strengths causing asymmetry towards bluer wavelengths.

We note that this object has been observed at only a single epoch, and so if WD J0103−0522 is a rotator, the sigma components may become visible when viewed from a more favourable orientation, permitting detailed analysis of the field structure.

WD J0412+7549 shows strong Balmer line core emission (see Fig. 4), hence, best-fitting parameters are omitted in Table 2. *Gaia* and Pan-STARRS agree on the photometric parameters ($T_{\rm eff}$ ≈ 8500 K and log g ≈ 8.25), which are likely more accurate. The object was observed on three consecutive nights (14–16 October 2018) and those show near-identical spectra with no obvious phase difference, which makes the possibility of a close double degenerate or a close irradiated low-mass companion rather unlikely. Furthermore, we made an attempt to simultaneously fit the spectroscopic and *Gaia* data using a composite of two white dwarf models, but no specific set of atmospheric parameters could provide a good match

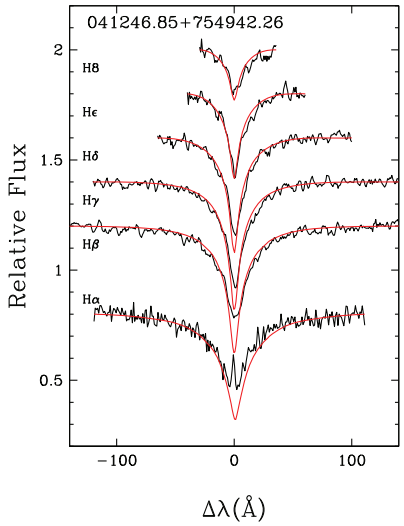

Figure 4. Comparison of the normalized observed Balmer line profiles for WD J0412+7549 with a DA model atmosphere at the *Gaia* derived photometric parameters ($T_{\rm eff}$ = 8510 K and $\log g$ = 8.25). Lines are offset vertically for clarity.

to the observations. In particular, the observed Balmer lines are fully inconsistent with two massive white dwarfs or a combination of a cool and hot white dwarfs, which would be required to explain the relatively small *Gaia* absolute fluxes. Therefore, we conclude that the observations show line emission that is likely to originate from or close to the white dwarf photosphere. We have verified that the object has 2MASS JHK and *WISE* W1 and W2 absolute fluxes consistent with a single white dwarf at the *Gaia* atmospheric parameters. This rules out a stellar companion, although, a late T-type brown dwarf (given the system cooling age of ≈1.5 Gyr) or giant planet would still avoid detection. The white dwarf is close (≈15 arcsec) to an edge-on dusty galaxy with an estimated redshift of z = 0.07 (Dálya et al. 2018). The redshift of the galaxy rules out that it is associated with the Balmer line emission, although it may complicate future efforts to obtain reliable IR observations of a possible companion.

WD J0620+4205 and *WD J1606+7022* are likely He-rich DA stars as they only show weak Hα lines, given their relatively warm photometric temperatures of 6300–6600 K (see Figs A8–A9). Binarity (DC+DA) is unlikely because both stars have photometric surface gravities close to or above the canonical $\log g$ = 8.0 value. From the equivalent width of the weak Hα lines at fixed *Gaia* atmospheric parameters, we find log(H/He) ∼ −2.5 for both objects. At the effective temperature of these white dwarfs, these large hydrogen abundances can be explained by either convective mixing (see fig. 16 of Rolland et al. 2018) or prior accretion of water-rich planetary debris (Raddi et al. 2015).

WD J0021+2531 and *WD J0129+5108* have problematic (non-WD like) Pan-STARRS photometry that does not agree with *Gaia* colours. *Gaia* agrees with the spectroscopic fits and therefore we favour these solutions.

WD J1613+4427, *WD J1809+2957*, *WD J1847+1226*, *WD J2004+0109*, and *WD J2253+8130* are each less than 30 arcsec from their bright G/K/M-star common proper motion companions, and the Pan-STARRS photometry is unreliable and likely contaminated. *WD J1929+1117* and *WD J1936+2632* are in crowded fields and Pan-STARRS photometry appears redder than expected from *Gaia* and spectroscopic parameters.

WD J0231+2859 and *WD J1923+2141* are likely DA+DA double degenerates as the photometric $\log g$ are much lower than the spectroscopic ones, despite unremarkable spectroscopic fits. Furthermore, both have photometric $\log g$ values in the range 7.50–7.70, consistent with two normal mass white dwarfs at similar temperatures.

4.2 DAZ white dwarfs

Fig. A5 shows the spectra of four new DAZ white dwarfs. Balmer line fits are shown in Figs A6–A7 for three of them, where the presence of metals at these cool temperatures is not expected to influence the Balmer line shapes. The very metal-rich *WD J0358+2157* is a notable discovery because it includes a large number of metal lines, possibly from different chemical elements. Given the relatively low temperature of 6600 K, the convection zone is large (Tremblay et al. 2015) and diffusion time-scales long (Koester 2009). Hence the total accreted mass must be relatively large, but there is no evidence that the white dwarf has a debris disc because the 2MASS JHK and *WISE* W1 and W2 absolute fluxes are consistent with the *Gaia* white dwarf parameters. This object will have a dedicated analysis in Gänsicke et al. (in preparation).

For *WD J1134+6108*, *WD J1749−2355*, and *WD J1802+1354*, we have measured Ca/H ratios (as well as Mg/H in the first case) using the model atmospheres of Koester (2010) and results are presented in Table 4. $T_{\rm eff}$ and $\log g$ were allowed to vary for internal consistency, but the atmospheric parameters were found to be similar to those otherwise derived in Table 2.

4.3 Magnetic white dwarfs

Fig. A12 shows eight magnetic white dwarfs, amongst which *WD J0303+0607* and *WD J2151+5917* were observed concurrently and recently analysed in Landstreet & Bagnulo (2019, 2020). Two further objects shown in the figure are new observations of known white dwarfs initially part of the Limoges et al. (2015) 40-pc sample. Both have a clear detection of Zeeman splitting at Hα. *WD J0537+6759* was already identified as possibly magnetic in Limoges et al. (2015), while *WD J0649+7521* is a new detection. There is also a new metal-rich magnetic white dwarf discussed separately in Section 4.5, and the likely magnetic ultra-massive DAH: white dwarf WD J0103−0522 discussed in Section 4.1, for a total of 9–10 new magnetic field detections not known before *Gaia* DR2.

WD J0303+0607 is already extensively discussed in Landstreet & Bagnulo (2020), where the authors detect a strong polarization signal. It has large absorption bands of unknown nature in the optical, hence we use the spectral type DXP. Landstreet & Bagnulo (2020) suggest that magnetic splitting of hydrogen lines from a huge (hundreds of MG) magnetic field is responsible for the observable features. The object is in a wide binary system and separated by only 11 arcsec from its close and bright G0V companion (Landstreet & Bagnulo 2020 estimate a physical separation of 380 au). As a result the *Gaia* fluxes have large error bars, while the Pan-STARRS photometry is unreliable. Combined with the lack of spectroscopic parameters, this results in rather uncertain atmospheric parameters for this object, although with a strong hint at a large mass ($1.18 \pm 0.15\,{\rm M}_{\odot}$), which is fully compatible with the mass determination in Landstreet & Bagnulo (2020).

We have found four DAH white dwarfs with obvious Zeeman splitting and average magnetic field strengths of ∼1 MG. *WD J2151+5917* is a cool white dwarf with a temperature of ≈5100 K, where only a weak Hα line is predicted. The line is tentatively split into three components separated by several angstroms,

Table 4. Atmospheric parameters and chemical abundances of hydrogen-dominated atmosphere metal-rich white dwarfs.

WD J name	SpT	$T_{\rm eff}$ (K)	log g	(Na/H)	(Mg/H)	(Ca/H)
013055.01+441423.29	DZA	4950 (20)	7.94 (0.02)	−8.99 (0.08)	–	−9.90 (0.07)
020210.60+160203.31	DZ	4910 (50)	8.13 (0.03)	–	–	−9.43 (0.03)
113444.64+610826.68	DAZ	7590 (40)	7.96 (0.02)	–	−6.79 (0.08)	−7.95 (0.04)
151534.80+823028.99	DZH	4490 (60)	7.90 (0.05)	−9.03 (0.02)	–	−9.72 (0.11)
174935.61−235500.63	DAZ	7430 (70)	8.03 (0.02)	–	–	−9.44 (0.15)
180218.60+135405.46	DAZ	8280 (70)	8.06 (0.05)	–	–	−8.81 (0.09)

Atmospheric parameters are based on an iterative fit of photometry and spectroscopy. All quoted uncertainties represent the intrinsic fitting errors.

Table 5. Field strengths for magnetic white dwarfs.

WD J name	SpT	$\langle B \rangle$ (MG)
030350.56+060748.75	DXP	>100
053714.90+675950.51	DAH	0.7 (0.2)
063235.80+555903.12	DAH	1.0 (0.2)
064400.61+092605.76	DAH	3.2 (0.2)
064926.55+752124.97	DAH	9.0 (1.0)
084516.87+611704.81	DAH	0.8 (0.2)
151534.80+823028.99	DZH	3.1 (0.2)
160700.89−140423.88	DAH	0.6 (0.2)
215140.11+591734.85	DAH	0.7 (0.2)

which has been confirmed in the meantime by Landstreet & Bagnulo (2019). For all magnetic white dwarfs, we estimate field strengths in Table 5 from Zeeman splitting but do not derive spectroscopic atmospheric parameters, which is notoriously difficult (Külebi et al. 2009).

4.4 DB and DC white dwarfs

We have found two DBA white dwarfs shown in Fig. A13. Both are at the very cool end of the DB range, where spectroscopic fits are difficult (Koester & Kepler 2015; Rolland et al. 2018). Using our 3D model atmospheres, we could derive spectroscopic parameters that are in reasonable agreement with *Gaia* values for *WD J0703+2534* with log(H/He) = −5.4 ± 0.3. For *WD J0552+1642*, the helium lines are too weak for a meaningful spectroscopic fit but we find a hydrogen abundance of the order of log(H/He) = −4.5.

The spectra of 76 DC white dwarfs are shown in Figs A14–A17. Only about a dozen have temperatures above ≈5100 K, where the helium-dominated nature of the atmosphere is unambiguous. A large number of these new white dwarfs have temperatures in the range 4800–5100 K, where H α is predicted to be marginal for pure-hydrogen composition. Higher S/N or higher resolution observations could be used to determine or confirm the atmospheric composition. The majority of new DC white dwarfs are cooler than 4800 K, where only detailed model atmosphere fits of the continuum fluxes could possibly suggest an atmospheric composition (Blouin et al. 2019b).

The analysis of *Gaia* and Pan-STARRS photometric fits of objects cooler than about 5000 K with either pure-H or pure-He model atmospheres, and with independent grids of models, has led to the finding that derived log g values are systematically lower by up to 0.1–0.2 dex compared to the average ≈8.0 value observed at higher temperatures (Hollands et al. 2018b; Blouin et al. 2019b, see also Paper II). This is also seen in Fig. 1 for the sample of new white dwarfs observed in this work. Since white dwarfs are expected to cool at constant mass even for that low-temperature regime (Tremblay et al. 2016), this is unlikely to be a real astrophysical effect. For a fixed mass–radius relation, apparent magnitude, and parallax, the photometric surface gravity correlates with effective temperature given Stefan–Boltzmann law, which implies that the issue could either be caused by *Gaia* temperatures that are too low or luminosities that are too large. In the former case, the amplitude of the colour correction necessary to obtain log $g \approx 8.0$ values would be fairly large ($G_{\rm BP}-G_{\rm RP} \approx 0.10$ mag) and vary strongly with temperature. It is unlikely to be a *Gaia* calibration issue and it is therefore unclear if this is at all related to the colour offset observed for warmer DA white dwarfs and discussed in Section 4.1, which is much milder. The issue is marginally worse with *Gaia* DR2 compared to Pan-STARRS (see Paper II) and as a consequence, we only use Pan-STARRS parameters for objects cooler than 4500 K.

WD J0639+2435 is in a wide binary with a bright F-star companion. Pan-STARRS photometry is contaminated as well as our red arm ISIS spectrum. Given the warm *Gaia* temperature of 8500 K and the lack of Balmer lines, we can nevertheless confirm that the atmosphere is helium dominated.

WD J1305+7022 and *WD J2305+3922* are rare examples of ultra-massive (1.19 and 1.13 $M_\odot$, respectively) and cool (4800 and 6500 K, respectively) DC white dwarfs. The former is cool enough that the atmosphere could be pure-hydrogen, while WD J2305+3922 is helium dominated with a relatively large upper limit on its hydrogen content (log(H/He) < −2.5). The progenitor of WD J2305+3922 could be a massive helium-rich DB white dwarf, which are rare (Tremblay et al. 2019a) but occasionally found (Richer et al. 2019). Alternatively, it could also have experienced convective mixing earlier in its evolution (Cunningham et al. 2020) or could be a cooled-down example of warm DQ white dwarfs (Coutu et al. 2019; Koester, Kepler & Irwin 2020) where carbon has diffused downward, for instance, from the shrinking of the convection zone or upwards diffusion of helium.

4.5 DZ white dwarfs

We show 10 new DZ and DZA white dwarfs in Fig. A18. We performed a combined spectroscopic and photometric analysis for the warmer subsample of these objects using the model atmospheres of Koester (2010) as described in Section 3. *Gaia* astrometry is used for all fits. In most cases we relied on multiple photometric data sets, including Pan-STARSS, SDSS, SkyMAPPER, UKIDSS, 2MASS, and *WISE*, but generally neglected broad-band *Gaia* photometry. We describe the data sets for individual objects below. We have added a systematic error, by forcing a reduced χ^2 of one, to account for possible systematic offsets between the various photometric surveys. Detailed fits are shown for the three most metal-rich objects in Fig. 5. The resulting atmospheric parameters and metal abundances

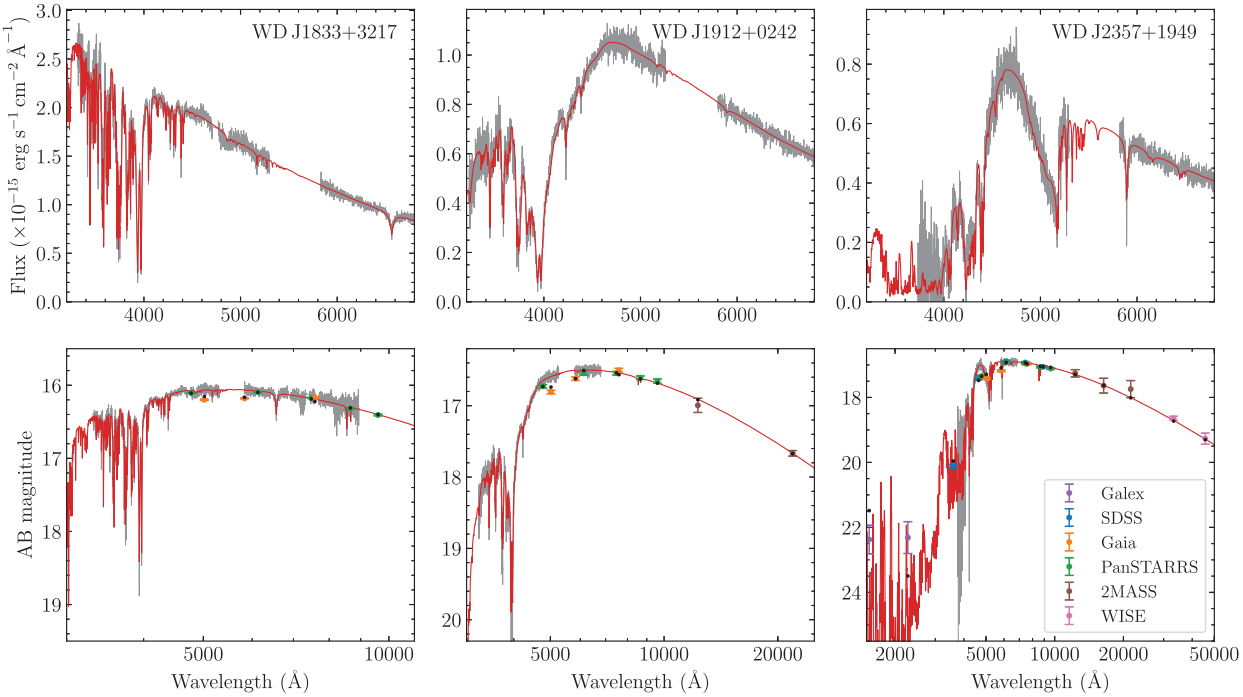

Figure 5. Simultaneous fits of spectroscopy and photometry for the DZA 183352.68+321757.25 (left-hand panels), DZ 191246.12+024239.11 (middle panels), and DZ 235750.73+194905.90 (right-hand panels). The top row of panels compare our best fit models to normalized spectroscopic observations. The spectroscopic observations are recalibrated on to the models to deal with flux-calibration quirks, but are still in physical flux units. The bottom panels compare our best fitting models to catalogue photometry over a wider wavelength range. All three objects have helium-dominated atmospheres and fit parameters are given in Table 6. For WD J1912+0242, the *K*-band is from UKIDDS rather than 2MASS.

are presented in Tables 4 (hydrogen-dominated atmospheres) and 6 (helium-dominated atmospheres).

WD J0130+4414 is a cool ≈5000 K DZA white dwarf with a weak H α line. Given the low temperature, the presence of hydrogen lines requires a pure-hydrogen atmosphere. The Ca H+K lines are also extremely narrow, confirming the atmospheric composition. The object has Pan-STARRS and SDSS photometry, both of which were used for the photometric fit. The spectrum shows a weak absorption feature from Na, which was not observed for the warmer DAZ stars discussed in Section 4.2. Compared to Ca, the Na abundance is large (see fig. 6 of Blouin et al. 2019a). We have verified that the Na detection is not from poor sky-subtraction. The line is broader than sky lines would be and the redshift is consistant with that of H α.

WD J0202+1602 exhibits a cool ≈4800 K DZ spectrum showing only lines from Ca I/II. The star has photometry from SDSS, Pan-STARRS, UKIDSS, and *WISE*, allowing model comparison across the full spectral energy distribution. Yet, in spite of the simple spectrum and ample photometric coverage, this object proved highly challenging to fit, and we consider our best attempts to constrain stellar parameters from a simultaneous fit of the photometric and spectroscopic observations to be unsatisfactory.

We found two solutions that were able to accurately reproduce either the spectrum or the photometry, but neither simultaneously. The first solution demonstrated a good fit to both the optical and infrared photometry, and required a cool hydrogen-dominated atmosphere (parameters listed in Table 4). However, the low pressure in this H-rich atmosphere results in Ca lines that are all too narrow (FWHM ≈ 3 Å in the model but ≈15 Å wide in the data). A better fit to the line widths can be achieved at a lower temperature (close to 4200 K), though the Ca I line becomes too strong relative to the Ca II doublet, and collision-induced absorption (CIA) from H_2–H becomes apparent in the model, but is not observed in the data.

While we note that a helium-dominated atmosphere (with next to no hydrogen), can also reproduce most of the photometry with similar stellar parameters, the Ca lines were found to be so highly broadened that such a possibility can be disregarded entirely. Instead, we find that a helium-dominated atmosphere with a moderate hydrogen component (log(H/He) = −1.46) can reproduce the spectrum well, though at a somewhat hotter $T_{\rm eff}$ (to maintain the Ca I/II line ratio) and higher log g (parameters listed in Table 6). For this He-rich solution, our photometric fit is extremely poor – the model overpredicts the optical flux by about 0.5 mag while underpredicting the infrared fluxes by a similar degree. Additionally, the model exhibits appreciable H_2–He CIA, while the observations do not. H_2–He CIA has been observed for other DZ stars, such as J0804+2239 which has a comparable $T_{\rm eff}$ and hydrogen abundance (Blouin et al. 2018). While Blouin et al. (2018) do find two photometric solutions for J0804+2239, these are either side of the H_2–He CIA maximum at log(H/He) = −2.5, with the higher hydrogen abundance solution also permitting an adequate spectroscopic fit. We advocate that the hydrogen-dominated solution is most likely to be correct, given its good agreement with all photometry and more typical surface gravity, though the reason for the overly narrow predicted Ca lines remains unexplained.

WD J0554−1035 has a He-atmosphere as it is warm enough to show Balmer lines if it was hydrogen dominated. The Ca H+K lines are very weak, suggesting there is very little opacity in this atmosphere. We fitted the Pan-STARRS and SkyMapper photometry and spectroscopy fixing the hydrogen abundance to log(H/He) = −4.0 throughout.

Table 6. Atmospheric parameters and chemical abundances of helium-atmosphere DZ and DZA white dwarfs.

WD J name	SpT	$T_{\rm eff}$ (K)	log g	(H/He)	(Na/He)	(Mg/He)	(Ca/He)	(Ti/He)	(Cr/He)	(Fe/He)	(Ni/He)
020210.60+160203.31	DZ	5380 (60)	8.40 (0.02)	−1.46 (0.03)	–	–	−9.43 (0.03)	–	–	–	–
055443.04−103521.34	DZ	6300 (40)	8.06 (0.02)	–	–	–	−11.82 (0.04)	–	–	–	–
183352.68+321757.25	DZA	7650 (60)	8.05 (0.02)	−3.31 (0.02)	–	−7.86 (0.04)	−8.72 (0.01)	−9.95 (0.05)	–	−7.08 (0.01)	−8.42 (0.03)
191246.12+024239.11	DZ	6050 (80)	8.15 (0.03)	−4.40 (0.17)	−9.70 (0.11)	−8.11 (0.01)	−9.11 (0.01)	–	–	−8.53 (0.01)	–
235750.73+194905.90	DZ	5700 (30)	7.95 (0.02)	–	−9.20 (0.02)	−6.79 (0.01)	−8.31 (0.01)	–	−9.29 (0.04)	−7.31 (0.02)	–

Atmospheric parameters are based on an iterative fit of photometry and spectroscopy. All quoted uncertainties represent the intrinsic fitting errors.

WD J1515+8230 is a cool ≈4500 K magnetic DZH for which abundance determinations are inherently more challenging. It likely has a hydrogen-rich atmosphere because the metal lines are much narrower than would be the case for a helium-dominated atmosphere at the same temperature. Because we are using non-magnetic models, the fit is only to the π-components, hence, we artificially increase the abundances by 0.48 dex to account for the other magnetic components. We find a magnetic field strength of 3.06 ± 0.14 MG.

WD J1833+3217 (Fig. 5) is a ≈7600 K DZA with a He-rich atmosphere, strong metal contamination, and obvious Balmer lines. The accreted material is found to be moderately Fe- and Ni-rich compared to known DZ stars (Hollands et al. 2017, 2018a) and the Balmer lines allow for a tight constraint on the hydrogen content of log(H/He) = −3.31 ± 0.02. The line blanketing was important to include in the atmospheric structure when fitting the Pan-STARRS photometry to obtain a consistent solution with spectroscopy. Note that while 2MASS and *WISE* photometry are available for this object, they are obviously contaminated by another source located <3 arcsec away, as shown by Pan-STARRS and *Gaia* data. Ca, Mg, and Fe abundances place the object firmly into the regime of polluted white dwarfs that are thought to have accreted material with core-Earth composition (see fig. 2 of Hollands et al. 2018a).

For the He-rich atmosphere *WD J1912+0242* (Fig. 5) we fitted against Pan-STARRS, 2MASS (*J*-band only) and UKIDSS (*K*-band only) photometry. The spectrum shows transitions from Na, Mg, Ca, and Fe. While hydrogen lines are not seen, leaving it as a free parameter does find a preferential value of log(H/He) = −4.40 ± 0.17.

For *WD J1922+0233,* we initially derived $T_{\rm eff} \approx 5800$ K and log $g \approx 9.10$ using *Gaia* photometry, which would imply the most massive polluted white dwarf known to date (Koester, Gänsicke & Farihi 2014; Coutu et al. 2019; Veras et al. 2020). However, a closer inspection of Pan-STARRS photometry reveals non blackbody-like optical fluxes sharply peaking in the *g* and *r* bands, with a drop-off in *i*, *z*, and *y* that is sharper than a Rayleigh–Jeans tail. This leaves the strong possibility that the object exhibits collision-induced absorption (CIA) with a spectrum close to that of so-called ultra-cool white dwarfs. This would make it the first DZ to show strong optical CIA absorption, although a few DZ are known to show strong near-IR CIA absorption (Blouin et al. 2019a). Our GTC spectrum only covers the red part of the optical spectrum and as a consequence only the sodium D-line is detected. Given the lack of near-IR photometry, we make no quantitative attempt to determine the atmospheric parameters. However, our preliminary analysis suggests that a hydrogen-dominated atmosphere and a very cool temperature is necessary to explain the sodium line. The lower temperature coupled with *Gaia* absolute fluxes would also suggest a more moderate mass for this white dwarf.

WD J2357+1949 (Fig. 5) is a relatively warm DZ with a particularly large Mg I triplet. This object benefits from having photometry from Pan-STARRS, SDSS, 2MASS, and *WISE*. We were able to fit five elements (Na, Mg, Ca, Cr, and Fe), with Si scaled with Mg, Ti with Ca, and Ni with Fe. The hydrogen abundance is largely unconstrained but must be low (log(H/He) < −6) to fit the lines and SDSS *u* band.

Finally, we postpone the detailed analysis of two of the coolest DZ white dwarfs, *WD J1824+1213* and *WD J2317+1830*, to a future work (Hollands et al., in preparation). These rare objects allow detailed microphysics study of cool and dense atmospheres in a way that is not possible with featureless DC objects (see, e.g. Blouin et al. 2019a).

Table 7. Atmospheric parameters and chemical abundances of DQ white dwarfs.

WD J name	SpT	$T_{\rm eff}$ (K)	log g	(C/He)
052913.45+430025.89	DQ	8580 (20)	7.94 (0.01)	−4.73 (0.03)
171620.72−082118.60	DQ	5800 (10)	7.73 (0.01)	−7.25 (0.02)

Atmospheric parameters are based on an iterative fit of photometry and spectroscopy. All quoted uncertainties represent the intrinsic fitting errors.

4.6 DQ white dwarfs

We show two DQ white dwarfs in Fig. A13. We fitted both objects with the model atmosphere code of Koester (2010) using an iterative procedure similar to that described for DZ stars. $T_{\rm eff}$ and log g rely mostly on the combined Pan-STARSS and *Gaia* photometry while C/He abundances are determined from the spectra. Results for both objects are shown in Table 7.

4.7 Non-white dwarfs

Fig. A19 and Table 8 show 12 high-probability white dwarf candidates ($P_{\rm WD} > 0.75$) from Gentile Fusillo et al. (2019) that turned out to be stellar objects. One additional source *WD J0456+6409* turned out to be a spurious *Gaia* detection and there is no object of that magnitude at the predicted location in Pan-STARRS or other sky images. In all other cases the *Gaia* source is real, isolated on the sky, and *Gaia* colours are confirmed by Pan-STARRS data. Most observed stars have G/K spectral classes and therefore are orders of magnitude over-luminous compared to where *Gaia* locates them in the HR diagram. The most likely explanation is that the *Gaia* parallaxes are greatly overestimated. The lower Balmer lines of WD J0727−0718 could be mistaken for a low-mass DAZ white dwarf, but a fit of the spectrum is consistent with an A-type main-sequence star. Considering the full sample of 521 confirmed *Gaia* white dwarfs in the Northern 40-pc hemisphere (Paper II), the contamination of the high $P_{\rm WD}$ sample is relatively small (1.3 per cent).

Table 8. Spectroscopically confirmed main-sequence stars.

WD J name	P_{WD}	Note
002332.98+432029.26	0.187	–
004940.60+033400.22	0.043	–
∗ 005645.62+551556.10	0.997	a, b
010343.47+555941.53	0.131	–
011519.50+573836.11	0.420	–
011608.20+584642.12	0.997	a, b
030433.12+361150.47	0.001	–
044454.33+632408.23	0.015	–
045620.38+640927.64	0.997	c
052129.02+185236.19	0.814	b
054615.88+380324.86	0.292	–
061350.39+010424.07	0.996	a
064643.38−090839.54	0.104	–
064711.68+243202.84	0.128	–
072714.16−071837.09	0.763	b
092138.08−014300.80	0.042	–
113726.34−112357.80	0.977	b
∗ 125256.54−140607.88	0.976	a
131843.05+381034.60	0.990	b
∗ 134252.41+003312.28	0.988	a
151421.37−110323.10	0.212	–
160430.57−192728.26	0.373	–
161105.78−045652.94	0.997	b
170027.28−184958.45	0.002	–
181747.59+191218.39	0.089	–
182431.36+193723.82	0.051	–
185136.02+221307.15	0.988	b
194333.65+222513.78	0.065	–
194530.78+164339.17	0.092	–
194843.46−073635.55	0.113	–
195513.90+222458.79	0.001	–
200748.71−040717.02	0.265	–
201437.22+231607.23	0.054	–
205009.26+291929.59	0.919	a, b
205241.82+294828.65	0.058	–
213132.74+332302.32	0.644	–
213723.27+224811.81	0.178	–
214756.33+225203.56	0.128	–
223544.75+391451.39	0.112	–

(a) high *Gaia* DR2 astrometric excess noise, (b) marked as duplicate source, (c) spurious *Gaia* DR2 source. Low probability white dwarf candidates ($P_{WD} < 0.75$) are intrinsically less reliable (Gentile Fusillo et al. 2019). Objects with an asterisk symbol have a parallax value outside of 40 pc but may still be within that volume at 1σ.

Nearly all the high-probability contaminants are flagged as *duplicated source*[3] in *Gaia* DR2, which is not taken into account in our probability calculation. This flag signifies that the detection system on-board *Gaia* generated more than one detection for these sources, but during on-ground processing those were identified as a single object and only one solution was kept. The parallax measurements for objects with the *duplicated source* seem to be inherently less reliable. However, ≈800 white dwarfs confirmed by SDSS spectroscopy can be correctly identified using their *Gaia* parallax despite having the *duplicated source* flag, indicating that it can not be used to efficiently eliminate unreliable sources in larger volume samples.

Fig. A20 and Table 8 show 26 stellar objects for which Gentile Fusillo et al. (2019) predict a low probability ($P_{WD} < 0.75$) of being a white dwarf. We emphasize that two more low probability candidates described in earlier sections turned out to be underuminous white dwarfs (WD J1305+7022 and WD J2317+1830), both with significantly larger proper motions than the average for low probability white dwarf candidates. This confirms that low probability candidates can still reveal some surprises although at a large observational cost, with only a few per cent of these objects turning out to be white dwarfs in this work. It is hoped that *Gaia* DR3 will help in defining a cleaner distinction between peculiar (under or overluminous) white dwarfs and contaminants.

[3]See chapter 10.2.2. of https://gea.esac.esa.int/archive/documentation/GDR2/index.html for information on the *duplicated source* flag.

5 SUMMARY

The volume-limited 20-pc white dwarf sample has long been a benchmark to study white dwarf evolution, stellar formation history, Galactic kinematics, the local binary population, and stellar magnetism (Giammichele et al. 2012; Tremblay et al. 2014; Holberg et al. 2016; Toonen et al. 2017; Landstreet & Bagnulo 2019). Thanks to *Gaia* DR2, the sample is now relatively well defined with a large spectroscopic completeness (Hollands et al. 2018b). Assembling a spectroscopically complete sample for the eight-times larger, 40-pc volume is a far greater challenge. Limoges, Lépine & Bergeron (2013), Limoges et al. (2015) initiated this important work by securing ≈300 spectra of new white dwarfs likely within 40 pc and mostly within the Northern hemisphere. We have pursued the goal of enhancing the spectroscopic completeness of the 40-pc sample by following-up 230 white dwarf candidates from *Gaia* DR2. We have described spectral types for 191 white dwarfs within that volume, in the vast majority confirmed as stellar remnants for the first time. We have reported on several examples of rare classes of white dwarfs, including a handful of ultra-massive remnants, a DA star with peculiar so-far unexplained Balmer line emission, one of the closest DZ white dwarfs accreting from a disrupted planetesimal with core-Earth composition and possibly the first ultra-cool DZ star.

We have now reached high-level spectroscopic completeness in the Northern 40-pc hemisphere. From cross-matching *Gaia* DR2 white dwarf candidates from Gentile Fusillo et al. (2019) with past spectroscopic catalogues (e.g. Limoges et al. 2015; Subasavage et al. 2017) and present observations, we identify 521 spectroscopically confirmed white dwarfs in the companion Paper II. Only three high-probability white dwarf candidates from Gentile Fusillo et al. (2019) do not have a spectral type in the northern 40-pc sample. The completeness of the *Gaia* DR2 catalogue itself and selection of Gentile Fusillo et al. (2019) are expected to be very high. Hollands et al. (2018b) estimate that *Gaia* DR2 has found at least 96 per cent of all white dwarfs within 20 pc and the completeness is expected to be similar within 40 pc, especially since the *Gaia* DR2 detection rate is poorer at very close distances (<10 pc) and high proper-motions (Hollands et al. 2018b). The northern 40-pc spectroscopic sample, an increase by a factor of 4 in size compared to the previous 20-pc sample, provides the observational constraints required to study, as outlined in Paper II, the mass, temperature, and age of white dwarf distributions, spectral evolution, properties of magnetic and metal-rich subtypes, the binary fraction, and the crystallisation of white dwarfs.

We have also contributed to enhance the spectroscopic completeness of the Southern hemisphere 40-pc sample, where observations are still underway. Including the 64 white dwarfs confirmed in this work, at least 320 white dwarfs in the southern 40-pc sample have a known spectral type, but there remains ≈200 high-probability candidates without spectroscopy, a sharp contrast with the Northern hemisphere. With upcoming multi-object spectroscopic (MOS) sur-

veys on 4-m-class telescopes such as WEAVE, 4MOST, and DESI, there is hope for a major increase in the size of volume-limited white dwarf samples. These surveys may take decades to cover the full sky, hence, the relevance of continued dedicated studies. However, magnitude-limited spectroscopic surveys in portions of the sky such as the SDSS (Kepler et al. 2019) can rival with volume-limited samples if biases and completeness are well understood.

ACKNOWLEDGEMENTS

The research leading to these results has received funding from the European Research Council under the European Union's Horizon 2020 research and innovation programme no. 677706 (WD3D). This article is based on observations made in the Observatorios de Canarias del IAC with the WHT operated on the island of La Palma by the Isaac Newton Group of Telescopes in the Observatorio del Roque de los Muchachos. Based on observations made with the Gran Telescopio Canarias (GTC), installed at the Spanish Observatorio del Roque de los Muchachos of the Instituto de Astrofísica de Canarias, in the island of La Palma. This work presents results from the European Space Agency (ESA) space mission Gaia. Gaia data are being processed by the Gaia Data Processing and Analysis Consortium (DPAC). Funding for the DPAC is provided by national institutions, in particular the institutions participating in the Gaia MultiLateral Agreement (MLA). BTG was supported by the UK STFC grants ST/P000495 and ST/T000406/1. ARM acknowledges support from the MINECO under the Ramón y Cajal programme (RYC-2016-20254), the AYA2017-86274-P grant, and the AGAUR grant SGR-661/2017. MRS thanks for support from Fondecyt (grant 1181404). DdM acknowledges financial support from ⟨0:funding-source 3:href="http://dx.doi.org/10.13039/501100003981"⟩ASI⟨/0:funding-source⟩-INAF I/037/12/0 and ASI-INAF no. 2017-14-H.0 and from INAF "INAF main streams", Presidential Decree 43/2018. RR has received funding from the postdoctoral fellowship programme Beatriu de Pinós, funded by the Secretary of Universities and Research (Government of Catalonia) and by the Horizon 2020 programme of research and innovation of the European Union under the Maria Skłodowska-Curie grant agreement no. 801370.

DATA AVAILABILITY STATEMENT

The raw data underlying this article are available in the ING Data Archives and The GTC Public Archive. The reduced spectra will be shared on reasonable request to the corresponding author.

REFERENCES

Bagnulo S., Landstreet J. D., 2019, MNRAS, 486, 4655
Beauchamp A., Wesemael F., Bergeron P., Fontaine G., Saffer R. A., Liebert J., Brassard P., 1999, ApJ, 516, 887
Bergeron P., Saffer R. A., Liebert J., 1992, ApJ, 394, 228
Bergeron P., Leggett S. K., Ruiz M. T., 2001, ApJS, 133, 413
Bergeron P. et al., 2011, ApJ, 737, 28
Bergeron P., Dufour P., Fontaine G., Coutu S., Blouin S., Genest-Beaulieu C., Bédard A., Rolland B., 2019, ApJ, 876, 67
Blouin S., Dufour P., Allard N. F., Kilic M., 2018, ApJ, 867, 161
Blouin S., Dufour P., Allard N. F., Salim S., Rich R. M., Koopmans L. V. E., 2019a, ApJ, 872, 188
Blouin S., Dufour P., Thibeault C., Allard N. F., 2019b, ApJ, 878, 63
Bond H. E. et al., 2017, ApJ, 840, 70
Brown W. R., Gianninas A., Kilic M., Kenyon S. J., Allende Prieto C., 2016, ApJ, 818, 155
Carrasco J. M., Catalán S., Jordi C., Tremblay P. E., Napiwotzki R., Luri X., Robin A. C., Kowalski P. M., 2014, A&A, 565, A11
Coutu S., Dufour P., Bergeron P., Blouin S., Loranger E., Allard N. F., Dunlap B. H., 2019, ApJ, 885, 74
Cui X.-Q. et al., 2012, RAA, 12, 1197
Cukanovaite E., Tremblay P. E., Freytag B., Ludwig H. G., Bergeron P., 2018, MNRAS, 481, 1522
Cukanovaite E., Tremblay P. E., Freytag B., Ludwig H. G., Fontaine G., Brassard P., Toloza O., Koester D., 2019, MNRAS, 490, 1010
Cunningham T., Tremblay P.-E., Gentile Fusillo N. P., Hollands M., Cukanovaite E., 2020, MNRAS, 492, 3540
Dalton G. et al., 2014, in Proc. SPIE Conf. Ser. Vol. 9147 Project Overview and Update on WEAVE. SPIE, Bellingham, p. 11
Dálya G. et al., 2018, MNRAS, 479, 2374
de Jong R. S. et al., 2019, The Messenger, 175, 3
DESI Collaboration et al., 2016, preprint (arXiv:1611.00036)
Fabricant D., Cheimets P., Caldwell N., Geary J., 1998, PASP, 110, 79
Fantin N. J. et al., 2019, ApJ, 887, 148
Fontaine G., Brassard P., Bergeron P., 2001, PASP, 113, 409
Fouesneau M., Rix H.-W., von Hippel T., Hogg D. W., Tian H., 2019, ApJ, 870, 9
Gaia Collaboration et al., 2018a, A&A, 616, A1
Gaia Collaboration et al., 2018b, A&A, 616, A10
Gänsicke B. T., Schreiber M. R., Toloza O., Fusillo N. P. G., Koester D., Manser C. J., 2019, Nature, 576, 61
Genest-Beaulieu C., Bergeron P., 2019, ApJ, 871, 169
Gentile Fusillo N. P. et al., 2019, MNRAS, 482, 4570
Gentile Fusillo N. P., Tremblay P.-E., Bohlin R. C., Deustua S. E., Kalirai J. S., 2020, MNRAS, 491, 3613
Giammichele N., Bergeron P., Dufour P., 2012, ApJS, 199, 29
Gianninas A., Bergeron P., Ruiz M. T., 2011, ApJ, 743, 138
Greenstein J. L., 1984, ApJ, 276, 602
Hamada T., 1971, PASJ, 23, 271
Henry T. J. et al., 2018, AJ, 155, 265
Holberg J. B., Oswalt T. D., Sion E. M., 2002, ApJ, 571, 512
Holberg J. B., Oswalt T. D., Sion E. M., Barstow M. A., Burleigh M. R., 2013, MNRAS, 435, 2077
Holberg J. B., Oswalt T. D., Sion E. M., McCook G. P., 2016, MNRAS, 462, 2295
Hollands M. A., Koester D., Alekseev V., Herbert E. L., Gänsicke B. T., 2017, MNRAS, 467, 4970
Hollands M. A., Gänsicke B. T., Koester D., 2018a, MNRAS, 477, 93
Hollands M. A., Tremblay P. E., Gänsicke B. T., Gentile-Fusillo N. P., Toonen S., 2018b, MNRAS, 480, 3942
Hollands M. A. et al., 2020, Nature Astron., 4, 663,
Jiménez-Esteban F. M., Torres S., Rebassa-Mansergas A., Skorobogatov G., Solano E., Cantero C., Rodrigo C., 2018, MNRAS, 480, 4505
Joyce S. R. G., Barstow M. A., Holberg J. B., Bond H. E., Casewell S. L., Burleigh M. R., 2018, MNRAS, 481, 2361
Kawka A., Simpson J. D., Vennes S., Bessell M. S., Da Costa G. S., Marino A. F., Murphy S. J., 2020a, MNRAS, 495, 129
Kawka A., Vennes S., Ferrario L., 2020b, MNRAS, 491, L40
Kemp J. C., Swedlund J. B., Landstreet J. D., Angel J. R. P., 1970, ApJ, 161, L77
Kepler S. O. et al., 2019, MNRAS, 486, 2169
Koester D., 2009, A&A, 498, 517
Koester D., 2010, Mem. Soc. Astron. Italiana, 81, 921
Koester D., Kepler S. O., 2015, A&A, 583, A86
Koester D., Schulz H., Weidemann V., 1979, A&A, 76, 262
Koester D., Gänsicke B. T., Farihi J., 2014, A&A, 566, A34
Koester D., Kepler S. O., Irwin A. W., 2020, A&A, 635, A103
Kollmeier J. A. et al., 2017, preprint (arXiv:1711.03234)
Külebi B., Jordan S., Euchner F., Gänsicke B. T., Hirsch H., 2009, A&A, 506, 1341
Landstreet J. D., Bagnulo S., 2019, A&A, 623, A46
Landstreet J. D., Bagnulo S., 2020, A&A, 634, L10
Leggett S. K. et al., 2018, ApJS, 239, 26
Liebert J., Bergeron P., Holberg J. B., 2005, ApJS, 156, 47

Limoges M. M., Lépine S., Bergeron P., 2013, AJ, 145, 136
Limoges M. M., Bergeron P., Lépine S., 2015, ApJS, 219, 19
Maíz Apellániz J., Weiler M., 2018, A&A, 619, A180
Manser C. J. et al., 2019, Science, 364, 66
Marsh T. R., 1989, PASP, 101, 1032
Marsh T., 2019, Astrophysics Source Code Library, record ascl:1907.012
McCleery J. et al., 2020, MNRAS, preprint (arXiv:2006.00874) (Paper II)
Motch C. et al., 1998, A&AS, 132, 341
Narayan G. et al., 2019, ApJS, 241, 20
Oswalt T. D., Strunk D., 1994, American Astronomical Society May Meeting Abstracts, 28.09
Raddi R., Gänsicke B. T., Koester D., Farihi J., Hermes J. J., Scaringi S., Breedt E., Girven J., 2015, MNRAS, 450, 2083
Rebassa-Mansergas A. et al., 2016, MNRAS, 463, 1137
Reid I. N. et al., 2004, AJ, 128, 463
Richer H. B., Kerr R., Heyl J., Caiazzo I., Cummings J., Bergeron P., Dufour P., 2019, ApJ, 880, 75
Rolland B., Bergeron P., Fontaine G., 2018, ApJ, 857, 56
Rowell N., 2013, MNRAS, 434, 1549
Scholz R. D., Meusinger H., Schwope A., Jahreiß H., Pelisoli I., 2018, A&A, 619, A31
Schreiber M. R., Gänsicke B. T., Toloza O., Hernandez M.-S., Lagos F., 2019, ApJ, 887, L4
Subasavage J. P. et al., 2017, AJ, 154, 32
Toonen S., Hollands M., Gänsicke B. T., Boekholt T., 2017, A&A, 602, A16
Tremblay P. E., Bergeron P., 2009, ApJ, 696, 1755
Tremblay P. E., Bergeron P., Kalirai J. S., Gianninas A., 2010, ApJ, 712, 1345
Tremblay P. E., Bergeron P., Gianninas A., 2011, ApJ, 730, 128
Tremblay P.-E., Ludwig H.-G., Steffen M., Freytag B., 2013, A&A, 559, A104
Tremblay P.-E., Kalirai J. S., Soderblom D. R., Cignoni M., Cummings J., 2014, ApJ, 791, 92
Tremblay P.-E., Ludwig H.-G., Freytag B., Fontaine G., Steffen M., Brassard P., 2015, ApJ, 799, 142
Tremblay P.-E., Cummings J., Kalirai J. S., Gänsicke B. T., Gentile-Fusillo N., Raddi R., 2016, MNRAS, 461, 2100
Tremblay P.-E., Cukanovaite E., Gentile Fusillo N. P., Cunningham T., Hollands M. A., 2019a, MNRAS, 482, 5222
Tremblay P.-E. et al., 2019b, Nature, 565, 202
van Maanen A., 1917, PASP, 29, 258
Vanderburg A. et al., 2015, Nature, 526, 546
Veras D., 2016, R. Soc. Open Sci., 3, 150571
Veras D., Tremblay P.-E., Hermes J. J., McDonald C. H., Kennedy G. M., Meru F., Gänsicke B. T., 2020, MNRAS, 493, 765
Winget D. E., Hansen C. J., Liebert J., van Horn H. M., Fontaine G., Nather R. E., Kepler S. O., Lamb D. Q., 1987, ApJ, 315, L77
Zuckerman B., Becklin E. E., 1987, Nature, 330, 138
Zuckerman B., Koester D., Melis C., Hansen B. M., Jura M., 2007, ApJ, 671, 872

SUPPORTING INFORMATION

Supplementary data are available at *MNRAS* online.

Appendix A. Figures A1–A20.

[1]*Department of Physics, University of Warwick, Coventry CV4 7AL, UK*
[2]*European Southern Observatory, Karl Schwarzschild Straße 2, D-85748 Garching, Germany*
[3]*Instituto de Astrofísica de Canarias, Universidad de La Laguna, E-38205 La Laguna, Tenerife, Spain*
[4]*Departamento de Astrofísica, Universidad de La Laguna, E-38206 La Laguna, Tenerife, Spain*
[5]*Institut für Theoretische Physik und Astrophysik, University of Kiel, D-24098 Kiel, Germany*
[6]*Smithsonian Astrophysical Observatory, 60 Garden Street, Cambridge, MA 02138, USA*
[7]*Institut de Recherche en Astrophysique et Planétologie, CNRS, Université de Toulouse, CNES, 14 Avenue Édouard Belin, F-31400 Toulouse, France*
[8]*Department of Physics and Astronomy, University College London, London WC1E 6BT, UK*
[9]*Space Sciences, Technologies and Astrophysics Research (STAR) Institute, Université de Liège, 19C Allée du Six Août, B-4000 Liège, Belgium*
[10]*Department of Astronomy, Boston University, 725 Commonwealth Avenue, Boston, MA 02215, USA*
[11]*Astronomisches Rechen-Institut, Zentrum für Astronomie der Universität Heidelberg, D-69120 Heidelberg, Germany*
[12]*Instituto de Física da Universidade Federal do Rio Grande do Sul, 91540 Porto Alegre, RS Brazil*
[13]*Gemini Observatory, 670 N'Aohoku Place, Hilo, HI 96720, USA*
[14]*INAF-Osservatorio Astronomico di Capodimonte, Salita Moiariello 16, I-80131 Naples, Italy*
[15]*Department of Physics and Astronomy, University of Sheffield, Sheffield S3 7RH, UK*
[16]*Institut für Physik und Astronomie, Universität Potsdam, Haus 28, Karl-Liebknecht-Strasse 24/25, D-14476 Potsdam-Golm, Germany*
[17]*Departament de Física, Universitat Politècnica de Catalunya, c/Esteve Terrades 5, E-08860 Castelldefels, Spain*
[18]*Institut d'Estudis Espacials de Catalunya, Edifici Nexus-201, c/Gran Capità 2-4, E-08034 Barcelona, Spain*
[19]*Key Laboratory of Space Astronomy and Technology, National Astronomical Observatories, Chinese Academy of Sciences, Beijing 100101, P. R. China*
[20]*Instituto de Física y Astronomía de la Universidad de Valparaíso, Avenue Gran Bretaña 1111, Valparaíso 2390302, Chile*
[21]*Millennium Nucleus for Planet Formation, NPF, Universidad de Valparaíso, Valparaíso 2390302, Chile*
[22]*INAF-Osservatorio Astrofisico di Torino, Strada dell'Osservatorio 20, I-10025 Pino Torinese, Italy*
[23]*Institute for Gravitational Wave Astronomy, School of Physics and Astronomy, University of Birmingham, Birmingham B15 2TT, UK*

This paper has been typeset from a TEX/LATEX file prepared by the author.